

1 **StageIV-IRC: A High-resolution Dataset of Extreme Orographic Quantitative**  
2 **Precipitation Estimates (QPE) Constrained to Water Budget Closure for**  
3 **Historical Floods in the Appalachian Mountains**

4 Mochi Liao<sup>1</sup> and Ana P. Barros<sup>1</sup>

5 1. Civil and Environmental Engineering, University of Illinois Urbana-  
6 Champaign, Urbana, IL

7 **Corresponding Author:**

8 Dr. Ana Barros

9 E-mail: [barros@illinois.edu](mailto:barros@illinois.edu)

10 Phone: +1 217-333-8038

11

Field Code Changed

## 12 **Abstract**

13 Quantitative Flood Estimation (QFE) in complex terrain remains a grand challenge in  
14 operational hydrology due to the lack of accurate high-resolution Quantitative Precipitation  
15 Estimates (QPE) for operational forecasting and for calibrating hydrologic models. Here, we  
16 present a high-resolution (i.e., 250m, 5-minute-hourly) QPE dataset for 215 extreme rainfall events  
17 occurred in 26 gauged mountainous basins in the Appalachian Mountains from 2008 to 2024. This  
18 dataset is developed by applying inverse rainfall corrections (IRC) derived from physically-based  
19 rainfall-runoff modeling (Liao and Barros, 2022 and 2023) to the Next Generation Weather Radar  
20 (NEXRAD) Stage IV analysis (4 km resolution, hourly). The corrected Stage IV analysis QPE is  
21 referred to as StageIV-IRC (StageIV with Inverse Rainfall Correction). The unique advantage of  
22 this StageIV-IRC QPE dataset is its agreement with ground-based rainfall measurements while  
23 achieving water budget closure at the storm-flood event scale and minimizing uncertainty from  
24 initial conditions using the Initial Condition Correction (ICC) module. ~~within observational~~  
25 ~~uncertainty of streamflow observations, which is the gold standard in hydrological modeling.~~ This  
26 dataset is the first QPE dataset aiming to improve QFE in the complex terrain by reducing biases  
27 for extreme precipitation events, and it can be used to evaluate the skill of hydrologic models in  
28 the same basins and support model calibration. The StageIV-IRC QPE dataset is publicly available  
29 at <https://doi.org/10.5281/zenodo.14028866>, and improved initial soil moisture maps for the  
30 studied extreme precipitation events, derived from the ICC module in the same IRC framework,  
31 are available in the same repository (Liao and Barros, ~~2025e~~2025c).

32

## 33 **1. Introduction**

34 Over the past few decades, extreme precipitation has become an increasingly important  
35 research topic due to its social, economic, and environmental impacts (e.g., Alimonti et al., 2022;  
36 Wernberg et al., 2013). Studies show that both total annual precipitation and extreme precipitation  
37 events have increased in the US and in other parts of the world during the last century (e.g., Milly  
38 et al., 2002), often resulting in floods (e.g., Pielke and Doughton, 2002), and flash floods in the  
39 context of complex terrain due to steep slopes (e.g., Schumacher, 2017; Czigány et al., 2010).  
40 Flash floods are characterized by fast rainfall-runoff responses on the scale of a few hours (< 6  
41 hours) after extreme precipitation events for watershed areas often ranging from a few tens to  
42 hundreds of square kilometers (e.g., Borga et al., 2014; Lumbroso and Gaume, 2012). As one of  
43 the deadliest natural hazards, flash floods are often associated with landslide events (e.g., Tao and  
44 Barros, 2014; Gupta et al., 2016; Deijns et al., 2022) and cause loss of life and property damage  
45 (Špitalar et al., 2014), such as recently in the last three years in the Appalachian Mountains, USA,  
46 and in Southern Spain. Despite extensive studies to improve flash flood simulations in small  
47 headwater basins, hydrological skill scores (e.g., Kling-Gupta Efficiency or KGE) remain poor at  
48 event scales largely due to significant difficulties involved in estimating highly localized  
49 orographic precipitation in complex terrain, which in turn implies that hydrologic models are not  
50 calibrated using forcing representative of realistic extreme events (e.g., Andrieu et al. 1997;  
51 Huffman et al., 2007; Mtibaa and Asano, 2022).

52 Current approaches involved in precipitation measurement and Quantitative Precipitation  
53 Estimation (i.e., QPE) broadly include in-situ point-scale observations using rain gauges and  
54 disdrometers, and remote spatial observations using ground-based radar and space-based sensors.  
55 In complex terrain, there is often a scarcity of in situ measurements due to difficult access. For

56 example, the rain gauge network from NASA's Integrated Precipitation and Hydrology Experiment  
57 is the only relatively dense rain gauge network installed at high elevations in the entire  
58 Appalachians (e.g., Barros et al. 2014). Other QPE products (e.g., radar QPE data) are plagued by  
59 uncertainties from various sources (e.g., ground clutter artifacts, retrieval uncertainties, and radar  
60 viewing geometry (Villarini and Krajewski, 2010; Arulraj and Barros, 2021; Kreklow et al., 2020;  
61 Huffman et al., 2007; Andrieu et al., 1997; Durden et al., 1998). Numerical weather prediction  
62 (NWP) is an alternative to measurement. However, QPE products from NWP models are  
63 characterized by significant uncertainties when evaluated against rain gauges (e.g., Zhang and  
64 Anagnostou, 2019), leading to large flood simulation errors when used as inputs to hydrological  
65 models, or introducing large structural uncertainty when used for model calibration (e.g., Tao et  
66 al., 2016; Weiland et al., 2015; Diomede et al., 2008; Kobold and Suselj, 2005). Due to these  
67 uncertainties and errors involved, focus has been directed towards enhancing QPE using various  
68 methods: data merging of raingauge and radar precipitation (e.g., McKee and Binns, 2016;  
69 Goudenhoofdt and Delobbe, 2009; Delrieu et al., 2014; Nanding et al., 2015; Sideris et al. 2013;  
70 Schiemann et al. 2011), combined radar reflectivity and retrieval corrections (e.g., Vignal et al.,  
71 2000; Shao et al., 2021; Dinku et al., 2002), and data assimilation into NWP models (e.g.,  
72 Rafiecinasab et al., 2015; Wehbe et al., 2020). Rain gauge and disdrometer measurements are often  
73 used as references for these QPE optimization approaches (e.g., Harrison et al., 2000; Shao et al.,  
74 2021; Fulton et al., 1998). The 'ground truth', however, has its own error (e.g., spatial  
75 representativeness, wind artifacts around the gauge orifice, and calibration, among others;  
76 Kochendorfer et al., 2017), and fails to capture highly localized orographic enhancement (e.g., Prat  
77 and Barros, 2010b; Gentilucci et al., 2021; Buytaert et al., 2006). Gauge-radar fusion often relies  
78 on geostatistical assumptions that are primarily distance-based (e.g., Areerachakul et al., 2022;

79 Cassiraga et al., 2021; Wang et al., 2020; Maggioni and Massari, 2018), lacking the full picture of  
80 complex basin topography, which has a regulating role in orographic precipitation processes.

81 To address this long-standing QPE challenge in complex terrain, a general QPE error  
82 quantification framework was developed leveraging widely available quality United States  
83 Geological Survey (USGS) streamflow observations at the outlet of headwater basins in complex  
84 terrain, consisting of 2 distinct paths: 1) rain gauge bias correction, and 2) grid-level QPE  
85 correction constrained to watershed-scale water budget closure. The first pathway includes rain  
86 gauge bias corrections at gauge locations both at the diurnal and climate scales, and the  
87 geostatistical distribution of rain gauge biases across a basin. The second pathway includes an  
88 innovative inverse QPE correction method by backward propagating runoff uncertainty using a  
89 hydrological model via streamlines to precipitation at storm-event scale, and the methodology is  
90 termed Inverse Rainfall Correction (IRC), which is developed by the same authors (Liao and  
91 Barros, 2022 or LB22). The IRC was initially developed in the Southern Appalachians and later  
92 extended to the headwater basins over a span of 2,000 km from south to north along the entire  
93 Appalachian Mountains for all headwater basins. It is worth noting that rain gauges are only  
94 available in the Southern Appalachians, thus elsewhere QPE corrections the StageIV product was  
95 downscaled to 250-m first and then submitted to the IRC without bias corrections or any other  
96 intermediate corrections as in LB22. in other headwater basins only went through the process of  
97 IRC without any prior rain gauge bias corrections. The generalizability of the IRC framework,  
98 regardless of rain gauge bias corrections beforehand, is demonstrated in is overall successful as  
99 documented in Liao and Barros (2023). (see Figure12).

100 LB22 found that initial soil moisture uncertainty causes inferior performance of IRC  
101 because large initial condition errors lead to significant uncertainties in travel time distributions.

102 Soil moisture is considered a particularly important factor among soil properties due to its  
103 significant role in affecting the generation of runoff, hence dramatically altering the timing of flood  
104 front and its magnitudes (e.g., Vivoni et al., 2007; Marchi et al., 2010; Penna et al., 2011), and soil  
105 moisture can vary dramatically at hourly timescales, changing from fully saturation levels to  
106 wilting point levels conditional on the specific texture and other properties of the soils (Grillakis  
107 et al., 2016). Initial soil moisture conditions can therefore determine whether a rainstorm produces  
108 a major flash flood or not (e.g., Komma et al., 2007; Zehe and Blöschl, 2004). However, due to  
109 the limited availability of soil moisture sensors, there are not many studies quantifying the impact  
110 of soil moisture on runoff simulation (e.g., Silvestro et al., 2019; Laiolo et al., 2016; Zappa et al.,  
111 2011; Uber et al., 2018). Liao and Barros (2025b) developed an Initial Condition Correction (ICC),  
112 which is based on travel time distributions and is coupled with the general IRC approach,  
113 demonstrating large improvements in initial soil moisture estimation. Note that when  
114 implementing the IRC and ICC, we are using a fully distributed physics-based uncalibrated model  
115 (i.e. Duke Coupled Hydrological Model, DCHM) that has been used successfully for more than  
116 two decades for hydrologic studies in the Southern and Central Appalachians (e.g., Tao and Barros,  
117 2013, 2014, 2018 and 2019; Tao et al. 2016; Yildiz and Barros 2004, 2007 and 2009), and  
118 consequently uncertainty from model structure and model parameters is assumed to be small.  
119 Hydrological model parameters certainly have an impact on rainfall-runoff response, but they are  
120 generally only of secondary importance compared to the precipitation proper and antecedent soil  
121 moisture distributions, especially for smaller basins (e.g., Dobler et al., 2012; Mockler et al., 2016).

122 In this work, IRC and ICC are combined into one ~~framework . structure~~ (referred to as the  
123 IRC-ICC framework ~~in Liao and Barros (2025b).~~) to construct an improved QPE dataset aiming  
124 to close the water budget at the scale of storm-flood events along the entire Appalachian Mountains

125 [ranges](#), (e.g., ~~Liao and Barros 2022 and 2025b~~). The study region is set to be the Appalachian  
126 Mountains because they are prone to extreme precipitation and flash floods due to orographic lift  
127 of moisture-laden air masses coming from the Gulf of Mexico and the Atlantic Ocean (e.g., Troch  
128 et al., 1994; Smith et al., 2011; Liao and Barros, 2023). A recent example is Hurricane Helene,  
129 which caused over 200 deaths and over \$50 billion in property damage in the Southeast US in  
130 September 2024. The IRC-ICC framework is employed in 26 headwater basins and 215 extreme  
131 events (during 2008-2024) using the Next Generation Weather Radar (NEXRAD) StageIV dataset  
132 as original inputs, at a spatial and temporal resolution of 250 m and 5 minutes, respectively, and  
133 the improved post IRC-ICC QPE data (i.e., StageIV-IRC) are made available in this study.

134 The manuscript is organized as follows. The data sources and the QPE error quantification  
135 framework, which consists of rain gauge bias correction and the IRC-ICC framework, are detailed  
136 in Section 2. Section 3 presents this new dataset (StageIV-IRC) along with data assessment from  
137 various aspects. Section 4 discusses the potential application of this new dataset and future work.  
138 Section 5 provides access to the dataset and a summary of the work.

139

## 140 **2. Data and Methodology**

### 141 **2.1 Radar QPE StageIV**

142 The NCEP/EMC StageIV is a precipitation estimation product, developed using hourly and  
143 6-hourly radar-rain gauge precipitation analyses at regional scales (Lin and Mitchell, 2005). In  
144 complex terrain, it is known that radar QPE suffers from the blockage of topography, overshooting  
145 and retrieval uncertainties, leading to large uncertainties in rainfall estimation. In 2007, as part of  
146 the ground validation (GV) of the Precipitation Measurement Missions (PMM) program by NASA

147 (e.g., Prat and Barros, 2010a and 2010b), 34 tipping bucket raingauges were installed in the  
148 Southern Appalachians and have been well-maintained since 2007 (e.g., Barros et al., 2014). In  
149 this work, rain gauge measurements from a GV rain gauge network ~~in the Southern Appalachians~~  
150 are utilized to reduce StageIV uncertainties in the Southern Appalachians.

151

## 152 2.2 GV Rain Gauge Observations

153 A rain gauge network in support of PMM GV was installed in the Pigeon River basin for  
154 the 10 year 2007-2018 period (Barros et al. 2014). A map of this rain gauge network is plotted in  
155 Figure 1. Every rain gauge is labelled with a number, and exact locations are documented in Table  
156 1. This rain gauge network is regularly visited and maintained at least three times a year, including  
157 on-site cleaning and calibration. In this study, these rainfall measurements are used as a basis to  
158 adjust hourly StageIV QPE. Note these rain gauge measurements can be downloaded at  
159 <http://dx.doi.org/10.5067/GPMGV/IPHEX/GAUGES/DATA301> (Barros et al., 2017). Besides  
160 rain gauges, a network of Parsivel disdrometers was installed during 2013-2014, with each  
161 disdrometer location denoted by the letter P in Figure 1. These disdrometer data were only used  
162 for independent evaluation because of short records. It is worth noting that rain gauges are installed  
163 mostly along the ridges while disdrometers are generally located at lower elevations.

164

165 <Figure 1 here please>

166

Formatted: Font: 11 pt, Italic

Formatted: Normal, Left, Indent: First line: 0", Space  
After: 0 pt, Line spacing: single

167 **2.3 Methodology**

168 The methodology of this work includes ~~four major elements~~~~three major components~~: a) rain gauge bias and climatology corrections where raingauge data are available, b) downscaling of radar precipitation, c) grid-scale QPE correction by closing the water budget using stream gauge measurements, and d) basin and event selection procedures and model setup.

172 **2.3.1 Rain Gauge Bias Corrections**

173 A schematic drawing of the rain gauge ~~bias~~-correction framework to derive gauge-improved QPE (named StageIV<sub>DBKC</sub>) is provided in Figure 2. ~~The~~ ~~where the~~ ~~subscripts~~ DBKC ~~referes to~~ 'Downscaled', 'Bias correction using rain gauge measurements at gauge locations', 'Correction from Kriging interpolation in 2D', and 'Climatological corrections', respectively.

177 <Figure 2 here please>

178

179 First, to make meaningful comparison between StageIV estimates and rain gauge measurements spatially s in spaae, a fractal downscaling algorithm is used to create StageIV<sub>D</sub> at 1km from the original StageIV at 4-km resolution. Subsequently, bias correction using raingauge measurements is employed to create StageIV<sub>DB</sub> at hourly timescales. StageIV<sub>DB</sub> data are then evaluated against the rain gauge climatology from 2008 to 2017 to reduce biases that depend on weather regime, and climatological biases are then spatially interpolated using the ordinary Kriging method. The resulting dataset is named StageIV<sub>DBKC</sub> (abbreviated as STIV<sub>DBKC</sub>).

186

- Formatted: Font: Bold, Underline

### 187 2.3.2 Fractal downscaling

188 The methodology for fractal downscaling was first proposed by Bindlish and Barros (1996)  
189 and subsequently demonstrated through various applications to precipitation downscaling from  
190 models (Bindlish and Barros, 2000) and remote sensing data (Nogueira and Barros, 2015; Tao and  
191 Barros, 2010). Here, a brief description is presented.

192 The assumption of self-similarity is imposed in fractal downscaling approach. The  
193 parameters used in this approach involve: fractal dimension  $D$ , Hurst coefficient  $H$ , and the spectral  
194 exponent  $\beta$  that are related through the following equations:

$$195 \quad D = \frac{7-\beta}{2} \quad (1)$$

$$196 \quad H = \frac{\beta-1}{2} \quad (2)$$

197 The parameter  $\beta$  describes rainfall statistics across different spatial scales, and it is  
198 calculated as the slope of the power spectral density curve in the 2D Fourier domain of the rainfall  
199 field (log-log plot). The parameter  $H$  is the Hurst coefficient which is a measure of autocorrelation  
200 strength with higher value representing stronger autocorrelation. The ~~power spectral density of a~~  
201 ~~2D field in Fourier domain~~ 2D Fourier transform of a rainfall field  $z(x, y)$  is calculated as the  
202 following:

$$203 \quad Z(u, v) = \left(\frac{L}{N}\right)^2 \sum_{x=0}^{N-1} \sum_{y=0}^{N-1} z(x, y) \exp\left[-\frac{2\pi i}{N}(ux + vy)\right] \quad (3)$$

204 where  $N$  is the total number of grid points of the rainfall field  $z(x, y)$  with grid size being  
205 the  $L$ ,  $u$  and  $v$  correspond to frequency indices in the Fourier domain in each direction. [Using Eq.](#)  
206 [3.4](#) the averaged power spectral density is given:

207 
$$S_j = \frac{1}{L^2 N_j} \sum_1^{N_j} |Z(u, v)|^2 \quad (4)$$

208 where  $N_j$  denotes the number of points that meet the following condition:  $j < \sqrt{u^2 + v^2} <$   
 209  $j + 1$ . ~~The mean power spectral density and the wavenumber  $k$  (Eq.5) are related by a power law (Eq. 6) and the mean power spectral density, and  $k$  is defined as below:~~

210 ~~There is roughly a power-law relationship between~~  
 211 ~~the wavenumber  $k$  (Eq.5) are related by a power law (Eq. 6) and the mean power spectral density,~~  
 212 
$$k = \frac{2\pi}{\sqrt{u^2 + v^2}} \quad (5)$$

213 
$$S \sim k^{-\beta-1} \quad (6)$$

214 ~~By applying a logarithmic transformation, the power-law relation between  $S$  and  $k$  is~~  
 215 ~~linearized, and Specifically, the corresponding  $S$  value when wavenumber  $k = 1$  is referred to as~~  
 216 the roughness factor, which is a representation of the variance of the field.

217 Assuming rainfall fields have self-similar statistics ~~from coarse resolution to fine resolution~~  
 218 ~~expressed by a power-law~~, then fine scale rainfall fields can be generated ~~from the coarse scale~~  
 219 ~~radar observations~~ by preserving these self-similar statistics. This is accomplished by creating a  
 220 Brownian surface at desired fine scale resolution while sharing the same spectral slope and  
 221 roughness factor as the original rainfall field based on Bindlish and Barros (1996):

222 
$$Z_D(u, v) = \frac{Z_b(u, v)}{k_r^{(\beta - \beta_b)/2}} \exp \left[ \frac{1}{2} \left( S_{r,1} - \frac{\beta + 1}{\beta_b + 1} S_{r,2} \right) \right] \quad (7)$$

223 where  $\beta$ ,  $\beta_b$ ,  $Z_D(u, v)$  and  $Z_b(u, v)$  are the spectral slope of 2D original rainfall field, the  
 224 spectral slope of the Brownian surface, interpolation surface in the Fourier domain and original  
 225 Brownian surface, respectively;  $k_r$  is the wavenumber and  $S_{r,1}$  and  $S_{r,2}$  are the roughness factors  
 226 of the 2D original rainfall fields and Brownian surface. Due to the non-uniqueness of Brownian

Formatted: Font: Italic

Formatted: Font: Italic

227 surfaces, multiple replicates of interpolation surfaces  $Z_D$  ~~must~~ ~~can~~ be ~~generated~~~~obtained~~. In this  
228 study, an ensemble of ND (~~Number of Downscaled samples~~) interpolation surfaces is derived ~~from~~  
229 ~~the original StageIV product where ND=50 following Nogueira and Barros (2015), and~~ thus ~~fifty~~  
230 ~~ND\_~~rainfall fields ~~realizations~~ at finer resolution preserving the same rainfall statistics at coarse  
231 resolution ~~is~~ ~~are~~ generated, and the ensemble mean was calculated. ~~In this work, a total of ND=50~~  
232 ~~ensemble downscaled rainfall fields are created similar to Nogueira and Barros (2015), and Finally,~~  
233 ~~a series of the~~ rainfall bias-correction steps ~~is~~ described in Figure 2 ~~are applied and is applied~~ to  
234 the ensemble mean of the downscaled rainfall fields.

235

### 236 2.3.3 ~~Climatology~~ Bias Corrections

237 The *first* phase of bias correction is carried out at the event scale: a linear regression is  
238 established between rain gauge measurements and collocated downscaled radar pixel estimates  
239 using the following formula:

$$240 R_g^t(i_g, j_g) = \kappa R_r^t(i_g, j_g) + \varepsilon \quad (8)$$

241 where  $R_r$  and  $R_g$  represent radar and rain gauge measurements respectively,  $\kappa$  and  $\varepsilon$  are the  
242 slope and the intercept of a polynomial fit between  $R_r$  and  $R_g$ . Hourly StageIV<sub>D</sub> estimates and  
243 corresponding rain gauge observations in the same StageIV<sub>D</sub> pixel were identified if at least 2 rain  
244 gauges in the same StageIV<sub>D</sub> pixel measure non-zero rainfall. A linear regression was applied to  
245 all StageIV<sub>D</sub> pixels within one standard deviation of the regression line at an hourly timescale by  
246 assuming homogeneity of variances or homoscedasticity.

247 The *second* phase of bias correction is done at decadal scale: aiming to reduce systematic  
248 radar errors caused by retrieval uncertainties and viewing geometry in complex terrain,

249 demonstrating strong diurnal (time of day) and seasonal (weather regime) error dependencies due  
250 to ~~missed~~ detection of shallow rainfall systems related to radar overshooting in the Southern  
251 Appalachian when comparing against 10-year rain gauge observations (e.g., [Prat and Barros,](#)  
252 [2010b](#); Wilson and Barros, 2014; [Duan et al. 2015](#); ~~Arulraj~~ and Barros, 2017). For this purpose,  
253 when rain gauge observations are  $< 2$ mm/hr and Stage IV<sub>D</sub> estimates are 0 mm/hr, the StageIV<sub>D</sub>  
254 value was automatically replaced by the rain gauge observations, which is referred to as the Light  
255 Rainfall Correction (LRC). Moreover, if StageIV<sub>D</sub> ~~rainfall intensity is zero estimates equal to 0~~  
256 where at least one collocated rain gauge observation is  $> 2$ mm/hr, then StageIV<sub>D</sub> estimates are  
257 replaced by the mean of all collocated rain gauge observations, namely Mean Rainfall Correction  
258 (MRC). Lastly, for highly localized precipitation (i.e., ~~fewer less~~ than 2 raingauges register  
259 nonzero rain in the study domain) which is normally ~~associated produced by with small-scale~~  
260 convective activity, the rainfall differences between the StageIV<sub>D</sub> and the local rain gauge  
261 observations were bilinearly distributed across nearby ~~25~~ grids (a 5x5 grid square centered at the  
262 StageIV<sub>D</sub> pixel) – Convective Rainfall Correction (CRC). For most of the raining hours, there are  
263 more than 2 rain gauges ~~with nonzero recorded rainfall~~, in which case the differences ~~at each~~  
264 ~~pixel~~ between radar estimates and raingauge measurements were spatially interpolated using  
265 ~~ordinary Kriging a geostatistical interpolation method (e.g., ordinary Kriging)~~, which is referred to  
266 as the Global Rainfall Correction (GRC).

267

### 268 2.3.4 Ordinary Kriging

269 Ordinary Kriging is a geostatistical interpolation method that generates artificial values of  
270 a variable at a specific location, aiming to minimize spatial variance. In this work, rainfall  
271 differences between raingauge observations and StageIV<sub>DB</sub> are calculated and distributed across

272 the entire basin using a spatial variance model, which is commonly referred to as a semi-variogram  
 273 model. Specifically, a spherical semi-variogram model is used. Literature regarding the choice of  
 274 semi-variogram models and their properties can be found (e.g., Li and Heap, 2008; Oliver and  
 275 Webster, 2015; Zimmerman and Zimmerman, 1991). Bohling (2005) pointed out that spherical  
 276 models reach the maximum variance for relatively shorter spatial lags, therefore more suitable to  
 277 capture highly nonlinear and localized orographic precipitation (McBratney and Webster, 1986):

$$278 \quad \gamma(h) = C_0 + (C - C_0) \left( \frac{3h}{2d} - \frac{1}{2} \left( \frac{h}{d} \right)^3 \right) \quad \text{if } 0 \leq h \leq d \quad (9.1)$$

$$279 \quad = C \quad \text{if } h > d \quad (9.2)$$

$$280 \quad \gamma_{0i} = \frac{1}{N_A} \sum_{k=1}^{N_A} \gamma_{ki} \quad (9.3)$$

$$281 \quad \gamma_{00} = \frac{1}{N_A} \sum_{k=1}^{N_A} \sum_{l=1}^{N_A} \gamma_{kl} \quad (9.4)$$

282 where  $h$  is the lag,  $d$  is the range,  $C$  and  $C_0$  are the sill and nugget values of the semi-variogram  
 283 model,  $N_A$  is the number of raingauges. The nugget is assumed to be zero if local variability and  
 284 measurement error are neglected at the point scales (Diggle and Ribeiro, 2007). The interpolated  
 285 rainfall difference at a location  $x_0$   $Z_{ok}^*(x_0)$  is calculated using a weighted combination of all  
 286 available differences at gauge locations  $G(x_i)$  multiplied by Ordinary Kriging weights  $\lambda_i^{ok}$ :

$$287 \quad Z_{ok}^*(x_0) = \sum_{i=1}^n \lambda_i^{ok} G(x_i) \quad (10.1)$$

$$288 \quad \sum_{i=1}^n \lambda_i^{ok} = 1 \quad (10.2)$$

289 Optimal Kriging weights can be obtained by a series of linear equations using the Lagrange  
 290 multiplier  $\mu$  method:

$$\begin{pmatrix} \gamma_{11} & \dots & \gamma_{n1} & 1 \\ \vdots & \ddots & \vdots & \vdots \\ \gamma_{1n} & \dots & \gamma_{nn} & 1 \\ 1 & \dots & 1 & 0 \end{pmatrix} \begin{pmatrix} \lambda_1^{OK} \\ \vdots \\ \lambda_n^{OK} \\ \mu \end{pmatrix} = \begin{pmatrix} \gamma_{01} \\ \vdots \\ \gamma_{0n} \\ 1 \end{pmatrix} \quad (11)$$

292 In this work, Ordinary Kriging interpolates differences between radar data and raingauge  
 293 observations to produce gauge-corrected STIV<sub>DBKC</sub> dataset. [An example sequence of rainfall fields](#)  
 294 [to illustrate the step-wise corrections described procedures mentioned in Sections 2.3.1-2.3.4 is](#)  
 295 [shown in Figure A1.](#)

### 297 2.3.5 Precipitation Assessment Metrics

298 Assessment metrics include the following: bias and root mean square error between radar  
 299 estimation and raingauge measurement, false alarm rate, the probability of detection ([PD](#)), threat  
 300 score ([TS](#)) and Heidlke skill score ([HSS](#)), following McBride and Ebert, 2000. An instance when  
 301 both radar QPE and rain gauge observation exceed a specified rain rate threshold is a hit (H); when  
 302 observation matches the criterion and radar QPE does not, it is classified as a miss (M); if the  
 303 opposite happens, then it is a false alarm (FA). The calculation of these metrics relied on a  
 304 collection of Hs, Ms, and FAs:

$$305 \quad Bias = \frac{1}{N} \sum_{n=1}^N (O_n - R_n) \quad (12)$$

$$306 \quad RMSE = \sqrt{\frac{1}{N} \sum_{n=1}^N (O_n - R_n)^2} \quad (13)$$

$$307 \quad FR = \frac{FA}{H+FA}, 0 \leq FR \leq 1 \quad (14)$$

$$308 \quad PD = \frac{H}{H+M}, 0 \leq PD \leq 1 \quad (15)$$

309 
$$TS = \frac{H}{H+FA+M}, 0 \leq TS \leq 1 \quad (16)$$

310 
$$HSS = 2 * \frac{Z * H - FA * M}{((H+FA) * (Z+FA)) + ((M+H) * (M+Z))}, -1 \leq HSS \leq 1 \quad (17)$$

311 where O is the rain gauge observation, R is the radar QPE, and N is the number of points. Z  
312 represent the number of zeros, meaning both raingauge and radar do not register a rainfall record  
313 above a predefined threshold. A threat score (TS) of 0.5 means over 50% of cases meet the  
314 criterion, and the higher the better. An HSS of 0 means a forecast has the same performance as a  
315 random guess.

316

### 317 **2.3.6 Inverse Hydrologic Correction**

318 At flash flood timescales in headwater basins, streamflow uncertainty and precipitation  
319 uncertainty are strongly connected in a nonlinear way through rainfall runoff processes. Liao and  
320 Barros (2022) developed a Lagrangian-based framework named Inverse Rainfall Correction (IRC),  
321 allowing backpropagating streamflow uncertainty to precipitation inputs in space and time through  
322 an uncalibrated distributed hydrological model (i.e., DCHM), achieving water budget closure at  
323 the event scale in small headwater basins. As stated earlier, the uncertainties associated with  
324 parameters and the hydrological model DCHM are neglected since the model configurations have  
325 been used and improved over the past two decades for this region accounting for various soil,  
326 vegetation, and river processes (e.g., Tao and Barros, 2013, 2014, 2018 and 2019; Yildiz and  
327 Barros, 2005 and 2007; Lowman and Barros, 2016), and the IRC framework has been tested in

328 multiple headwater basins extensively in this region with consistent success. The detailed  
329 description of the IRC is provided in Section 2.3.8 and Appendix A.

330 It is worth noting that IRC is a general framework to improve QPE at the watershed scale  
331 that can be incorporated into any distributed hydrological models. Liao and Barros (2025a, 2025b)  
332 investigated the impact of model structure uncertainty and initial condition uncertainty on IRC and  
333 then the downstream product: the resulting IRC\_-improved QPE. The results suggest with  
334 improved watershed physics at finer resolution (e.g., river bank storage, Liao and Barros, 2025a),  
335 river routing algorithms (e.g., XY routing, Liao and Barros, 2025a) and improved antecedent soil  
336 moisture distributions (Liao and Barros, 2025b), post-IRC QPE demonstrate realistic precipitation  
337 features at high resolution that are aligned with basin topography with ridges associated with  
338 higher precipitation than valleys in general, showing a significant improvement from the original  
339 StageIV dataset which is characterized by unnatural boxy precipitation patterns in complex terrain  
340 due to resolution issues and over or underestimation depending on topography and distance from  
341 the radar site.

342 As briefly mentioned before, LB22 reviewed various sources of uncertainty that can  
343 prevent post-IRC QPE from achieving water budget closure, among which initial condition  
344 uncertainty in soil moisture is a noteworthy source. Improved initial condition estimation results  
345 in significantly improved post-IRC precipitation features in complex terrain by better capturing  
346 transient travel time distributions (Liao and Barros, 2025b). They found that the uncertainty tied  
347 to initial conditions is more significant for less extreme events. Nevertheless, the initial condition  
348 correction method is coupled with the IRC framework, and the complete framework is named the  
349 IRC-ICC framework. The specifics regarding the IRC, ICC, and IRC-ICC are schematically drawn  
350 in Figure 3.

351

352 <Figure 3 here please>

353

354 Using the definitions of characteristic timings shown in panels c) and d), characteristic flow  
355 regime windows are identified. In principle, the number and the size of the windows depend on  
356 the complexity of the hydrograph. ICC is only applied to windows 2 and 5 in this example, which  
357 represents a segment of the hydrograph characterized by the differences between rising points in  
358 observations and simulations, and a segment characterized by slow recession, respectively. The  
359 assumption is that precipitation uncertainty regulates streamflow differences during peak flows  
360 (i.e. windows 3 and 4).  $W_{nm}$  represents the framework state after window  $m$  for iteration  $n$ . The  
361 resolution settings for the DCHM are: spatial resolution: 250m, and temporal resolution: 5 minutes.

### 362 **2.3.7 Implementation of Lagrangian Tracking**

363 A flood event is simulated by the DCHM at the basin outlet with grid-based time-varying  
364 velocity fields for different soil layers. When the precipitation starts (i.e. basin-averaged  
365 precipitation  $> 0.1\text{mm/hr}$ ), new particles (passive tracers) are launched at the same frequency of  
366 model temporal resolution (5 minutes), but only at non-zero precipitation grids in all soil layers  
367 following the velocity fields calculated by the DCHM, and the tracking resolution is 10 seconds,  
368 amounting to a release of approximately 600,000 particles for basin with an area of  $120\text{km}^2$  over  
369 a 24-hour period. During the tracking phase, each particle is saved along with information  
370 regarding its source location (grid-point where it originates), time of release  $t_i$ , and travel time  $t_T$   
371 ( $t_T$  is defined as the difference between current time  $t$  and the time of release  $t_i$ , i.e.,  $t_T = t - t_i$  ).  
372 Multiple particles from different source locations can have the same travel time, which is the basis

373 for identifying the number of trajectories contributing to the hydrograph at the outlet as a function  
374 of time.

375

### 376 **2.3.8 QPE Correction Using IRC**

377 At time  $t$ , the water difference  $wd(t)$  between the observed and simulated streamflow over  
378 the time  $\Delta t$  between two consecutive discharge observations represents the fraction of runoff that  
379 eventually leaves the basin as streamflow. Errors in precipitation forcing propagate to the runoff,  
380 under the assumption of negligible model and parameter uncertainties,  $wd(t)$  can be entirely  
381 attributed to precipitation error, which is the focus of this work.

$$382 \quad wd(t) = [Q_{obs}(t) - Q_{simu}(t)] \times \Delta t \quad (18)$$

383 The subscripts *obs* and *simu* refer to observed and simulated discharge, respectively.  
384 The strategy for the inverse rainfall correction (IRC) using hydrograph analysis is to follow the  
385 trajectories available from the Lagrangian tracking backward from the basin outlet to the source  
386 locations at time  $t_i$  and apply a correction at the source locations proportional to the original QPE  
387 magnitude to reduce  $wd$  at time  $t$ . Detailed formulas with a conceptual drawing can be found in  
388 Appendix A. The embedded assumption is that larger QPE values have larger uncertainties. Note  
389 that QPE corrections that happened earlier in time will have an impact on runoff simulation at  
390 future times, and this is the reason why the IRC framework is a recursive framework. The detailed  
391 rainfall correction steps can be found in (Liao and Barros, 2022).

392

393 **2.3.9 Methods for Reducing Uncertainties from Other Sources**

394 As briefly mentioned before, uncertainties from other sources (e.g., model physics, model  
395 numerical formulation, antecedent soil moisture conditions, etc.) impact travel time distributions  
396 and simulated streamflow to a higher or lesser degree depending on location, antecedent  
397 conditions, and storm system. Previous studies demonstrate that, for flood-producing events in  
398 small headwater basins, streamflow response is largely controlled by precipitation inputs (e.g.,  
399 Iwasaki et al., 2020). In this section, we briefly describe the methods used to minimize the impacts  
400 from other sources to enhance water budget closure using the IRC approach.

401 As discussed in the Introduction DCHM has been used in the Appalachian Mountains at  
402 event-scale (e.g., Tao and Barros, 2013, 2014, 2018 and 2019; Tao et al. 2016) and at seasonal and  
403 interannual scales (Yildiz and Barros 2005, 2007 and 2009), and thus extensive analysis of  
404 parameter uncertainty and model structure uncertainty has been conducted previously. Recent  
405 improvements to the flood routing algorithm have resulted in significant improvements in flood  
406 peak timing in headwater basins to reconcile the hydraulics of flood wave propagation on steep  
407 slopes at the highest elevations with milder slopes at intermediate elevations in the valleys (Liao  
408 and Barros, 2025a). Their results also suggest meandering effects, riverbank storage, and initial  
409 soil moisture distributions can impact the early rising period of the hydrographs. Significant and  
410 consistent improvements are made when introducing an initial condition correction (ICC) module  
411 to reduce initial condition uncertainty (Liao and Barros, 2025b). This innovative ICC module is  
412 coupled with the IRC framework. The red arrows in Figure 3e indicate where ICC is executed in  
413 the general architecture of the IRC framework, and the specifics of the ICC module are described  
414 below.

415 Particles launched during the IRC process that reached the outlet at time  $t$  are traced back  
416 directly to the IC timing or time 0, and their locations at the IC timing are shown in the bottom  
417 maps in Figure 3d (referring to control points of time  $t$ ). The downstream area of the control points  
418 has shorter transportation time to arrive at the outlet (e.g., water difference  $\Delta S_1$ ), and the upstream  
419 area of the control points takes longer to get to the basin outlet (e.g., water difference  $\Delta S_2$ ).  
420 Similarly, soil moisture in the impacted area can greatly impact the size of  $\Delta S_2$  and flow conditions  
421 after the timing  $t_2$ . Assuming initial conditions are only impactful during the early period and late  
422 recession of the hydrograph, which is supported by the fact that these events are flood-producing  
423 events with large QPE uncertainties dominating the vicinity of peak flow, ICC is used for  
424 hydrological windows outside the peak flow windows. Following the same notation (backward-  
425 in-time) in the IRC framework (Eq. 18),  $wd(t)$  is calculated as the flow volume difference  
426 between observed and simulated streamflows for the time interval defined by  $t$  and  $t - \Delta t$ . A  
427 ‘band’ of region can therefore be identified, that is, a region formed by control points of time  $t$   
428 and control points of time  $t - \Delta t$ . This ‘band’ is then referred to as the impacted area of initial soil  
429 moisture for time  $t$ , meaning basin discharge between time  $t - \Delta t$  and time  $t$  is impacted by initial  
430 soil moisture at the delineated impacted area. Finally,  $wd(t)$  is then converted to soil moisture  
431 content and added to initial soil moisture within the impacted area (i.e. the ‘band’) and the details  
432 can be found in Liao and Barros (2025b).

433

### 434 2.3.10 Hydrological Skill Metrics

435 The Kling-Gupta Efficiency (KGE) is calculated using observed and simulated streamflow  
436 statistics at observation resolution  $\tau$  (here 15 minutes) in this work:

437 
$$KGE_{\tau} = 1 - \sqrt{(r - 1)^2 + \left(\frac{\sigma_{sim}}{\sigma_{obs}} - 1\right)^2 + \left(\frac{\mu_{sim}}{\mu_{obs}} - 1\right)^2}$$
 (19)

438 where  $r$  is the correlation between simulations and observations,  $\sigma_{obs}$  is the standard  
 439 deviation of observed discharge,  $\sigma_{sim}$  is the simulated discharge standard deviation,  $\mu_{sim}$  and  
 440  $\mu_{obs}$  represent the average simulated and observed streamflow values, respectively.

441 The relative volume error (EV) is the relative difference between simulated flood volume  
 442 and observed flood volume:

443 
$$EV = \frac{V_{sim} - V_{obs}}{V_{obs}}$$
 (20)

444 Where V stands for volume of the flood. An  $EV > 0$ , and an  $EV < 0$  mean overestimation and  
 445 underestimation, respectively.

446 EPT refers to the error in peak flow timing between observations and simulations. For its  
 447 calculation, only the highest peak is selected for calculating EPT if more than one peak is present.  
 448 In this work, EPT is determined by considering the entire flood rising limb to account for the  
 449 steepness of the rising limb, specifically, both the flood starting timing and the maximum flood  
 450 timing from the flood front rising limb are used for calculating the EPT.

451 EPV or error in peak volume ( $Q_{max}$ , cubic meters per second) is a relative error calculated  
 452 using peak flows from observations and simulations, and the equation is below:

453 
$$EPV = \frac{Q_{max_{sim}} - Q_{max_{obs}}}{Q_{max_{obs}}}$$
 (21)

454

455 **2.3.11 Study Domain and Model Setup**

456 ~~Twenty-eight~~An initial 30 gauged headwater basins with areas and quality streamflow  
457 records were are identified selected from south to north along in the Appalachian Mountains  
458 (Figure 4, Table 3). s as illustrated in Figure 1, with basin drainage area ranging from 50 km<sup>2</sup> to  
459 500 km<sup>2</sup>. It is demonstrated in Figure 4 that these basins scatter across the entire Appalachians.  
460 For example, Basin01 and Basin30 are over 2,000 km apart, with diverse weather and climate  
461 regimes, and large differences in geomorphology and hydrogeology. The smallest basin (Basin 07)  
462 and the largest basin (Basin 12) were discarded because their areas were less than 20 km<sup>2</sup> and  
463 greater than 600 km<sup>2</sup>, respectively due to being too small for IRC at 250 m resolution and too  
464 large for IRC due to complex hydrologic response from different catchments not all impacted by  
465 the same rainfall event, significantly different than other basins. Note that an additional 2 basins  
466 (Basin 13 and 14) were later discarded from inclusion in the final data set as explained later in  
467 Section 3.2 and Section 3.2.1. Therefore, making the final published StageIV-IRC product  
468 includes 26 basins and 215 events in 26 basins.

Formatted: Superscript

469  
470 <Figure 4 here please>

471  
472 Soil-related parameters ~~were~~are downloaded from a global high-resolution (1 km) soil data  
473 repository (Zhang et al., 2018). For each basin, the vertical hydraulic conductivity remains the  
474 same for the entire soil column. The lateral hydraulic conductivity in the unsaturated zone was  
475 assumed to be two to three orders of magnitude larger than the vertical conductivity in the shallow  
476 soil layers, with higher values where the stone fraction in the soils is higher (Carlson, 2010; Freeze

477 and Cherry, 1979). The final scaling factors were obtained through simple sensitivity analysis to  
478 match the curvature and slope of the observed subsurface runoff recession curves (e.g., Linsley et  
479 al., 1982; Chen and Kumar, 2001; Yildiz and Barros, 2007), and scaling factors are finally  
480 determined as: 1500, 150, 15 and 1.5 for layer 1 (0-10 cm below terrain surface), layer 2 (10-75  
481 cm below terrain surface), layer 3 (75-200 cm below terrain surface) and layer 4 (2-20 m below  
482 terrain surface), respectively. No parameter optimization is done in this work, as the primary focus  
483 of this work is to develop a QPE dataset that can consistently close the water budget while  
484 controlling uncertainties from other sources, largely advancing the understanding of QPE  
485 uncertainties across climate, weather, and geomorphological regimes.

486 Flood-producing events ~~were have been~~ selected for ~~the 28~~<sup>28</sup> ~~twenty eight~~ headwater basins  
487 ~~with areas ranging between 50-500 km<sup>2</sup>-~~ (Table 3) for recent years from January 2021 to April  
488 2024. A qualified event is determined based on the observed peak flow, which must surpass 95%  
489 of available flow measurements for each basin. The choice of 95% is a compromise because 99%  
490 would yield too few events, while 90% would be too close to the annual flood. Additionally,  
491 rainfall runoff response time must be shorter than or equal to 6 hours to be qualified as a flash  
492 flood event. Only warm season precipitation events from 2021 to 2024 are finally considered.  
493 Here, the warm season is specifically defined as from April 1st to September 30th. Note: data  
494 quality control is enforced, and events with missing streamflow records are discarded.

495 For the Cataloochee Creek Basin (Basin05), located in the SAM known to have  
496 experienced multiple flash floods in the past (Tao and Barros, 2013 and 2014), Liao and Barros  
497 (2023) created a Historical Flood Record database (HFR) that includes a large number of extreme  
498 rainfall events from 2008 to 2017. The event selection criteria when developing HFR also use the  
499 same 95% flow threshold method. The difference is that the HFR also includes multiple winter-

Formatted: Superscript

500 time liquid precipitation events that result in cold-season flash floods. In total, there are 54 warm-  
501 season events for Basin 05 in HFR, and these events are also used to expand the study sample size  
502 in this work.

503 To ~~initialize~~~~warm-up~~ the DCHM, a traditional spin-up approach is used with iterative runs  
504 for the hydrological year of 2021 (from the end of April to the end of September), and it generally  
505 reaches equilibrium after 3-5 iterations. Subsequently, DCHM is continuously running from the  
506 beginning of October 2021 onwards, to derive initial conditions for events after September 30th,  
507 2021. During this spin-up process, no parameter calibration is involved. The initial conditions are  
508 extracted from the last iteration of spin up run, and the following model outputs generated after  
509 October 1<sup>st</sup>, 2021.

#### 510 **2.4 Caveats**

511 In the entire study domain, rain gauges are only installed in the Southern Appalachians,  
512 specifically in the vicinity of the Cataloochee Creek Basin (Basin 05). However, the rest of the  
513 regions are not equipped by raingauge networks, and therefore, no rain gauge bias correction is  
514 done for those basins, and the downscaled original dataset StageIV (i.e., STIV<sub>D</sub>) is used as input  
515 for the IRC method and hydrological simulations in this study.

516 As an important component of the IRC framework, the Lagrangian tracking algorithm is  
517 only implemented when hydrological window changes, rather than following model temporal  
518 resolution (i.e., 5 minutes), due to practical computational constraints. Additionally, we do not  
519 differentiate peak flow points and recession inflection points between simulations and observations  
520 when classifying hydrological flow regimes/windows, and consistently use observations delineate  
521 hydrological windows simply because 1) particle locations are inherently much more uncertain  
522 when simulation time is getting longer partially due to numerical truncation errors and grid-based

523 abruptly-changing velocity fields used in the Lagrangian tracking algorithm, and 2) the  
524 computational costs of the tracking algorithm. Very short travel times (i.e., <15 minutes) are  
525 ignored because of temporal resolution restrictions from streamflow observations. A systematic  
526 use of 24 hours for event total duration is imposed in this work to reduce excessive tracking  
527 workload, which might be problematic for events with very long and heavy tails, though not  
528 common for flash flood events in headwater basins.

529 The IRC-ICC recursive framework allows us to quantify QPE uncertainties more  
530 realistically by improving initial soil moisture estimation, and this framework is numerically  
531 efficient in terms of reaching hydrological equilibrium state within 3-5 iterations. In this work, the  
532 stable state of IRC-ICC is reached when the KGE changes are bound by 0.05.

### 533 **3. Results and Discussion**

#### 534 **3.1 Rain gauge Bias Correction**

535 The climatologically corrected  $STIV_{DBKC}$  fields have a significantly accurate diurnal cycle  
536 compared to only event-scale bias-corrected  $STIV_{DBK}$ . This process is illustrated in Figure 5 for  
537 one rain gauge from each side of the ridges (eastern side: left panel; western side: right panel) in  
538 the Southern Appalachians.

539

540 <Figure 5 here please>

541

542 Original  $StageIV_D$  show higher biases over the western ridges (e.g., right panel) for all hours of  
543 day, illustrating the difficulties of capturing seeder-feeder enhancement of low-level precipitation

544 systems (Duan and Barros, 2017). Also, the mid-day dry bias has been a problem for radar  
545 measurements in this region. (e.g., Barros and Arulraj, 2019). Results show that StageIV<sub>DBKC</sub>  
546 datasets capture precipitation climatology better with smaller missing detection errors compared  
547 to original StageIV. Figure 6 shows the diurnal characteristics of the missing percipitaaion for  
548 two raingauge locations for winter season (January-February and March – JFM) using StageIV,  
549 and this phenonemon is observed for both the StageIV<sub>D</sub> (black) and StageIV<sub>DBK</sub> (cyan). These  
550 missing cases correspond to light rainfall that have small rainfall measurements at rain gauge  
551 locations (< 1.5 mm/hr, bottom row). After applying precipitation climatology corrections, the  
552 missing issue in StageIV<sub>DBK</sub> is significantly alleviated and much better results are shown in  
553 StageIV<sub>DBKC</sub> fields (green).

554

555 <Figure 6 here please>

556

557 The seasonal HSS, TS, and RMSE of STIV<sub>DBKC</sub> are significantly better than those of  
558 STIV<sub>D</sub> throughout the day using 10-year averages (Figure 7a). It is worth noting with increasing  
559 precipitation rate threshold (Figure 7b), threat score does not show decreasing trend, meaning  
560 raingauge bias correction for heavy rainfall events works well. Figure 7c shows RMSE  
561 performance conditional on rain rate at diurnal and seasonal scales. Overall, the RMSE is generally  
562 less than 0.1 mm/hr except in the cold-season morning and late afternoon, which can be partially  
563 attributed to snow events because these raingauges are not heated.

564

565 <Figure 7 here please>

566

### 567 **3.2 Hydrologic Correction**

568 The coupled IRC-ICC was originally developed and applied in Basin 05, the Cataloochee Creek  
569 Basin, and an example showing the results from iterations is demonstrated in Figure 8. The  
570 notation follows the definition in Figure 3. Note that the  $STIV_{DBKC}$  data derived in Section 3.1 are  
571 further downscaled to 250m and used for hydrological simulations in this section. For all other  
572 basins (except Basin05), rain gauges are not available, and  $STIV_D$  data are used instead.

573

574 <Figure 8 here please>

575

576 It is demonstrated that IRC-ICC produces stable results after about 3 to 4 iterations without  
577 significant oscillations for this specific extreme flood event. In general, for less significant events,  
578 IRC-ICC reaches equilibrium faster (merely three iterations), providing fast and convergent  
579 corrections. As explained earlier, the equilibrium state is reached and thus IRC-ICC is stopped  
580 when oscillations in simulated KGE are within 0.05, and then IRC-ICC is stopped immediately.  
581 This study suggests that for most events, three iterations is a good rule of thumb. The difference  
582 between the initial 4D (x, y, z, t) rainfall forcing and the final result of the IRC-ICC is the general  
583 IRC correction.

584

#### 585 **3.2.1 Systematic Application of IRC-ICC**

586 The IRC-ICC is systematically executed in the 28 basins located in the Appalachians for  
587 225 events, and examples are displayed in Figure 9.

588

589 <Figure 9 here please>

590

591 Simulated streamflows generally have better performances in the Northern and Southern  
592 Appalachian Mountains (NAM, SAM) compared to the Central (CAM). Specifically, in the Karst  
593 region along the interstate border of Virginia and West Virginia in the CAM, for Basins 13 and  
594 14, where there are numerous caverns and natural tunnels facilitating fast subsurface flow response,  
595 that is, sinking and subterranean streams ([https://www.dcr.virginia.gov/natural-](https://www.dcr.virginia.gov/natural-heritage/vacavetrail)  
596 [heritage/vacavetrail](https://docslib.org/doc/2284608/west-virginia-tax-districts-containing-karst-terrain) and [https://docslib.org/doc/2284608/west-virginia-tax-districts-containing-](https://docslib.org/doc/2284608/west-virginia-tax-districts-containing-karst-terrain)  
597 [karst-terrain](https://docslib.org/doc/2284608/west-virginia-tax-districts-containing-karst-terrain)). The current version of the DCHM does not have a specific module designed for  
598 karst geology and karst hydrological processes. Thus, the IRC-ICC results in these locations are  
599 impacted by model structural uncertainty. Here, the advantage of not calibrating model parameters  
600 becomes apparent. It would be possible to calibrate model parameters to improve model  
601 simulations; however, the physical basis and transferability of the IRC-ICC results would be  
602 compromised. The 10 events in Basins 13 and 14 are therefore discarded (example: Figure A43).  
603 This point of discussion is highlighted here to reinforce the value of the data set presented in this  
604 manuscript for applications with other hydrologic models, including model calibration, where  
605 model structural uncertainty is not a primary concern at resolved scales.

606 Event 2021-06-10 in Basin 19 (see Figure A43) is an example of an event with a complex  
607 hydrograph (e.g., multiple minor flood peaks around one major flood peak) that requires more  
608 hydrological windows (see Figure 3). Subtle changes in the hydrograph shape could be indicative  
609 of spatial shifts in runoff production from one tributary to another following the track of storm  
610 cells over the basin. Indeed, depending on the weather system and regional topography, the travel

611 velocity of such cells and their life-cycle may require finer spatial and temporal resolution both  
612 for the hydrological model and for the tracking algorithm to capture changes in the spatial structure  
613 of precipitation, especially in the case of summer thunderstorms. For the systematic production of  
614 this data set, a 5-window IRC-ICC framework was applied, including a pre-rising-point segment,  
615 rising limb, early recession, and late recession (separated by the recession inflection point).

616

### 617 **3.2.2 IRC and IRC-ICC Precipitation Corrections**

618         Accumulated rainfall totals per rainfall event are calculated for both the IRC-only product  
619 and post IRC-ICC products. Subsequently, these rainfall totals are directly compared against  
620 original product  $STIV_{DBKC}$ . Examples are shown in Figure 10, categorized by seasons in the  
621 Cataloochee Creek Basin (Basin05). Again, the warm season is defined as April 1st to September  
622 30th, and the remaining events are defined as the cold season, with only liquid precipitation events  
623 studied in this work.

624

625 <Figure 10 here please>

626

627         The original QPE (**a1** and **b1**) shows abrupt changes in rainfall intensity, which is a  
628 common issue of radar observations at high spatial resolution. On the contrary, the IRC-corrected  
629 precipitation maps demonstrate precipitation features aligning with landform, showing strong  
630 spatial precipitation gradients along ridges and adjacent valleys (examples are listed in Figure A32).  
631 The spatial correlation between orographic precipitation and topography is observed across all  
632 mountain ranges, including the Appalachians (e.g., Konrad II, 1994; Smith et al., 2011; Wolvin et

633 al., 2024). Note the dark blue colors in Figure 10 corresponding to very low precipitation near the  
634 basin outlet are an artifact of the IRC tied to very short travel times that cannot be fully resolved  
635 even at fine scales of 250m and 5minutes. However, these artifacts are much reduced for the IRC-  
636 ICC due to the reduction of uncertainty in initial conditions, as shown for the 2009-10-14, 2009-  
637 04-20, and 2013-04-12 events because of overall basin-wide travel time improvement. It is worth  
638 noting that these three events are relatively mild events, indicating a larger impact of IC on  
639 relatively less extreme events because of the critical role of IC in runoff generation mechanisms  
640 and travel times distributions. Thus, the extreme event precipitation product obtained from IRC-  
641 ICC is the data set recommended for applications with other hydrologic models.

642

### 643 3.2.3 Precipitation and Hydrologic [Skill Metrics Statistics](#)

644 Event-total precipitation maps are calculated for each basin and event, and basin-scale  
645 precipitation statistics (e.g., mean and standard deviation) are derived for each event-total  
646 precipitation map. These statistics are plotted in Figure 11, and subregions are separated by vertical  
647 black lines. Basins 01 to 11 are located in the SAM, Basins 12 to 20 are located in the CAM, and  
648 Basins 21 to 30 are located in the NAM. Basins 13 and 14 are not included in the statistics.

649 <Figure 11 here please>

650 It is clearly demonstrated that the change in the mean (i.e., basin-averaged event total QPE)  
651 is relatively small (from 36.10mm to 38.07mm) compared to the change in the standard deviation  
652 (from 6.63mm to 14.08mm) after the application of IRC-ICC. The small standard deviation of the  
653 original QPE suggests that the original QPE data are spatially tightly clustered with low variability  
654 (see Figure 10a for boxy rainfall features), while the larger standard deviation post-IRC-ICC

655 indicates spatial variability is enhanced, which is highlighted by the terrain-aligned precipitation  
656 features in Figure 10c. The relatively small change in the mean indicates that the original input  
657 precipitation (i.e., StageIV<sub>DBKC</sub> for Basin 05, and StageIV<sub>D</sub> for the remaining basins) does not  
658 contain significant unconditional systematic biases across basins and events, which would lead to  
659 consistent positive or negative flood volume errors. As an exception, it is worth noting that the  
660 standard deviation of Basin 05 events does not change significantly after the IRC-ICC compared  
661 to other basins and events because rain gauge corrections from the IPHEX network are employed  
662 in Basin 05 but not anywhere else. It can never be overly emphasized that even after rain gauge  
663 bias correction, essentially a point-scale correction method, the resulting flood hydrograph exhibits  
664 significant water budget closure errors (see Figure 12 for more discussion) on account of the high  
665 heterogeneous nature of QPE in complex terrain.

666 The hydrologic statistics described in Table 1 using all studied events are plotted in Figure  
667 12.

668 <Figure 12 here please>

669 Figure 12 shows that the median KGE across events is improved from 0.36, 0.39, 0.27 to  
670 0.89, 0.74, 0.84 for SAM, CAM, and NAM, respectively. It should be pointed out that QPE  
671 changes for Basin 05 events (event numbers 55 to 108) are important for improving water budget  
672 closure, albeit small in magnitude compared to other events in other basins, as shown in Figure 11  
673 and 12, and yet critical to capture the complex precipitation heterogeneity in complex terrain to  
674 close the water budget. The results for Basin 05 illustrate the limitations of rain gauge-based bias  
675 corrections in complex terrain in general. The relatively small improvement shown in the CAM is  
676 partially attributed to the fact that DCHM does not have a proper representation of subterranean  
677 rivers in karst terrain, causing large baseflow errors during hydrograph recession and thus low

678 KGE values. Nevertheless, for flash flood applications, peak flow magnitude, flood flow timing,  
679 and event flow volume are the most important forecast objectives, corresponding to the 2<sup>nd</sup>, 3<sup>rd</sup>,  
680 and 4<sup>th</sup> horizontal panels in Figure 12. Overall, flood volume error (EV) is controlled within  $\pm 10\%$   
681 for over 90% of the studied events (the 2<sup>nd</sup> panel), with the median EV error being less than 5% in  
682 the SAM and NAM after IRC-ICC corrections. Flood peak volume (the 3<sup>rd</sup> panel) is generally  
683 controlled within 20%, which is very good for extreme events in regions without ground-based  
684 observations except for radars placed far away. This is demonstrated by Tropical Storm Fred on  
685 2021-08-17: an event that caused floods in multiple SAM basins, caused five deaths, and resulted  
686 in an economic loss of more than 1 billion dollars. Note the KGE for this event is improved to 0.9,  
687 and peak timing errors are  $<30$  minutes using IRC-ICC. Timing errors (shown in the 4<sup>th</sup> subplot)  
688 are bounded by  $\pm 60$  minutes for the major of the events for post IRC-ICC datasets, though some  
689 outliers exist potentially due to complex antecedent land surface physics (e.g., rain on snow) for  
690 April events, particularly in the CAM and NAM.

691 Events associated with significant timing errors (more than  $\pm 90$  minutes) are investigated  
692 in detail. These include the 2023-07-08 event (event number 185) for Basin 27, which is located  
693 in New Hampshire (the estimated flood front occurs too early by 2.5 hours). This was a localized  
694 summer thunderstorm event, only taking 30 minutes to reach its peak flow. The fast changes in the  
695 hydrological regime require much more windows than the current classic 5-window settings used  
696 in the IRC-ICC framework. The event on 2022-05-27 (event number 118) in Basin16 located in  
697 West Virginia is characterized by a slow rising limb. Note Basin16 is partially located in a complex  
698 region with karst features (e.g., sink holes) in the Greenbrier-river valley. Finally, the event 2021-  
699 09-22, a complex rainfall system characterized by multiple rain cells passing through the Basin 19  
700 quickly (event number 133), requiring smaller hydrological windows to capture highly variable

701 rainfall-runoff responses than the 5-window default IRC-ICC architecture: baseflow segment, pre-  
702 rising segment, flood rising limb, early and late recession.

703 Overall, large improvements in QPE are achieved, resulting in hydrological improvements  
704 in aspects of peak magnitude, flood total volume and flood front timing. Due to the dependence of  
705 IRC-ICC on travel time distributions, it cannot be used when precipitation is missing or there are  
706 severe timing errors because of the lack of water travel time trajectories to distribute corrections.  
707 From a practical point of view, the QPE IRC-ICC correction is in nature a type of space-time bias  
708 correction. The improved QPE data facilitates the development of QPE error models, which is  
709 demonstrated by the same authors (e.g., Liao and Barros, 2023), providing a path towards  
710 correcting remote-sensing products to support hydrometeorological studies and advancing the  
711 calibration of hydrological models with significantly less forcing uncertainty.

712

#### 713 **3.2.4 Independent Verification**

714 As mentioned in the introduction, precipitation measurements are limited in the Appalachians  
715 except for the IPHEX rain gauge network (Figure 1). Currently, the NEXRAD radar network  
716 remains the widely used precipitation monitoring system in this region in spite of well-documented  
717 low radar quality coverage over radar gaps in the mountains. The Multi-Radar/Multi-Sensor  
718 (MRMS) product (Zhang et al., 2016), which is developed using NEXRAD radar measurements  
719 similar to StageIV, is created at 1km resolution and is used here for independent verification.

720 First, original MRMS data are downscaled to the same resolution as StageIV<sub>D</sub> datasets (250m,  
721 5min) and used as inputs for DCHM. Hydrological simulations in this section are using the same  
722 model configuration and initial model states for the purpose of a meaningful comparison, including

723 the following datasets: MRMS<sub>D</sub>, StageIV<sub>D</sub>, and IRC-ICC StageIV<sub>D</sub> as shown in Figure 13. Figure  
724 13a shows that MRMS and StageIV QPE have similar results. Second, the IRC-ICC StageIV<sub>D</sub>  
725 have generally a good agreement with MRMS<sub>D</sub> similar to StageIV<sub>D</sub>. However, for some cases,  
726 where rainfall is dramatically underestimated by the radar system and KGE values are low, IRC-  
727 ICC is shown to provide effective corrections. Otherwise, the IRC-ICC generates physically  
728 constrained corrections spatially (see Figure 10), achieving high KGE values for flood simulations.  
729 Figure 13b shows the histogram of the KGE values across different rainfall products for all events.  
730 Overall, simulated streamflows using MRMS<sub>D</sub> and StageIV<sub>D</sub> exhibit similar hydrologic  
731 performance (the median KGE across events is close to 0.20), on the contrary, post-IRC-ICC  
732 StageIV<sub>D</sub> produce flood simulations with a median KGE above 0.80.

733

#### 734 **4. Discussion and Future Work**

735 Limitations in this study stem mainly from computational constraints rather than  
736 methodology. A default 24-hour flood duration window is imposed, implying that for long-lasting  
737 floods, due to significant slow interflow and baseflow contributions, are not considered. The  
738 current version of the IRC-ICC framework was built to support flash flood studies and only targets  
739 shallow subsurface moisture transport, given the critical importance of shallow soil moisture on  
740 the regulation of flood generation and propagation in steep terrain. It is worth noting that for long-  
741 lasting rainfall events or regions with relatively flat terrain, slow interflows would become more  
742 important in terms of regulating flood timing, flood volume, and post IRC-ICC QPE.

743 While the IRC results could be further optimized if carried out at the same frequency as  
744 the model resolution, therefore eliminating any artifacts due to inadequate sampling and updating

745 of travel time distributions, and while there is room to improve the IRC-ICC framework through  
746 improved model physics and resolution, utilizing 3D velocity fields to capture the full travel time  
747 distributions, and using different models to generate IRC ensembles. to test and calibrate  
748 hydrologic models for an intercomparison study, advancing flood forecasting skill, and to support  
749 emergency management response.

750

## 751 5. Data Availability Statement

752 The StageIV-IRC dataset at 250 m 5-minute resolution for 26 basins and 215 events is  
753 available at: <https://doi.org/10.5281/zenodo.14028866>. (Liao and Barros, 2025c), excluding  
754 Basin 07 (the smallest basin), 12 (the largest basin), 13 (Karst terrain), and 14 (Karst terrain) based  
755 on previous discussion. Associated geographic documentation of the selected basins is also  
756 provided via the same link. Initial soil moisture distributions for the studied events are also  
757 available in the same Zenodo repository.

758 The StageIV-IRC precipitation data consist of precipitation fields at 250m every 5 min for  
759 each event and headwater basin. The StageIV radar product was first downscaled from 4km to  
760 250m using fractal downscaling, resulting in STIV<sub>D</sub>. Hourly data were linearly interpolated to 5  
761 minutes. The IRC-ICC framework was applied to STIV<sub>D</sub> to derive the StageIV-IRC product that  
762 is made public for all events across all basins except for Basin 05. Because high quality data are  
763 available from rain gauge network in Basin 05 since 2007, a series of precipitation corrections  
764 based on these data was applied to the STIV<sub>D</sub> data including event-scale bias correction, decadal-  
765 scale bias correction, and ordinary kriging. The resulting data is STIV<sub>DBKC</sub>. For Basin 05, the IRC-  
766 ICC framework was applied to STIV<sub>DBKC</sub>.

Formatted: Subscript

Formatted: Subscript

Formatted: Subscript

Formatted: Subscript

Formatted: Subscript

767 This work relies on an uncalibrated distributed hydrologic model to simulate rainfall-runoff  
768 response. Model parameters are obtained from the literature and from publicly available datasets.  
769 The key assumption in this work is that precipitation uncertainty of extreme events dominates over  
770 other hydrologic uncertainty tied to model structure and model parameters. Consequently,  
771 differences between simulated and observed hydrographs at stream gauge locations are attributed  
772 to precipitation errors upstream in the contributing watershed.

773 This work is expected to work the best for heavy precipitation events that are typically  
774 associated with large precipitation measurement and estimation uncertainties. It is recommended  
775 that readers should address uncertainties in precipitation estimation at watershed scale before  
776 parameter calibration in hydrologic modeling studies.

777

## 778 **6. Conclusion**

779 QPE has been an enduring challenge in hydrology, particularly in complex terrain. Ground-  
780 based radar QPE is plagued with uncertainties from multiple sources, while rain gauge networks  
781 are scarce and suffer from the lack of representativeness in the mountains. To address this grand  
782 challenge, we develop a series of corrections from point-scale to watershed-scale encompassing  
783 event bias, climatology, and water budget closure: the IRC-ICC framework. To our knowledge,  
784 this is the first QPE dataset that meets standard statistical evaluations against point-based  
785 measurements where available and meets water budget closure at flood-event scale, consistent  
786 with nonlinear rainfall-runoff processes in headwater basins, and achieves superior hydrological  
787 performance at sub-hourly.

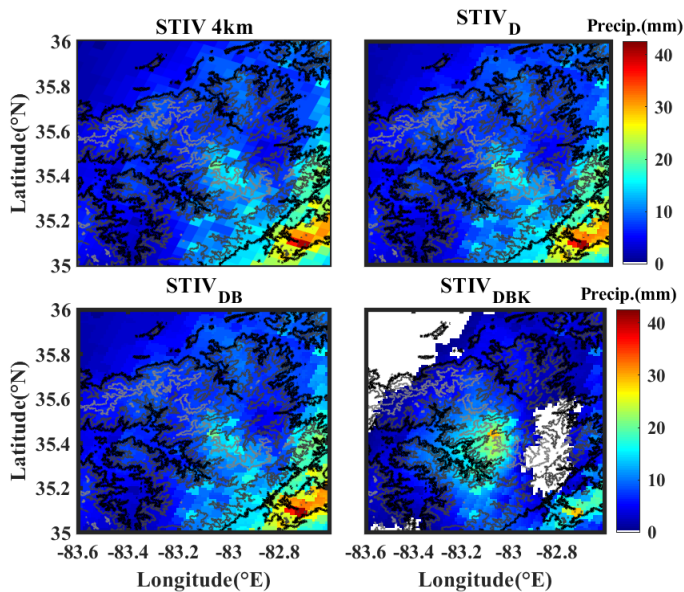
788           The IRC-ICC framework is successfully adopted in 26 mountainous basins (excluding the  
789 basins that are heavily overlapped with Karst terrain) in the Appalachians for 215 events with  
790 robust success, yielding substantial improvements of streamflow simulation, particularly in terms  
791 of flood volume and timing. The tracking algorithm in the IRC-ICC framework is only updated  
792 when shifting from one hydrological window to another, but not every time step. With enough  
793 computational resources, post-IRC-ICC QPE data should further improve by capturing transient  
794 travel time distributions between model time steps.

795           When using the StageIV-IRC product, flood timing errors are controlled with one hour for  
796 90% of events, compared to less than 20% when using original StageIV, while the median KGE  
797 improved from 0.34 to 0.86 across the events. This change in KGE is achieved by significant  
798 changes in the space-time variance of precipitation that in turn impacts the space-time variability  
799 of rainfall-runoff processes. Results illustrate the importance of initial conditions for less severe  
800 rainfall events, particularly during the beginning of the event, which influences subsequent  
801 streamflow simulations. It should be emphasized that physical parameters are not calibrated for  
802 any precipitation event in any basin in this work. This physics-based IRC-ICC framework can  
803 capture the fundamental physics involved in flash flood events: essentially the fast rainfall-runoff  
804 responses in surface and shallow subsurface layers; therefore, skillful hydrologic prediction is  
805 achieved without model calibration. Instead, the focus is on getting the forcing right.

806           The IRC-ICC is a general framework that can be incorporated into any distributed  
807 hydrological model. Thus, the StageIV-IRC dataset also enables meaningful intercomparison  
808 among different radar QPE datasets, providing physics insights into QPE error structure from a  
809 water budget closure perspective, toward improving radar retrievals and to characterize radar-  
810 specific errors related to radar operations at high spatial resolution in the mountains. The

811 demonstrated success of StageIV-IRC in ungauged basins strongly supports the use of IRC-ICC  
 812 in mountainous regions worldwide, where rain gauges are generally not available. Further, this  
 813 dataset can be utilized as a reference for building machine learning models (or even deep-learning  
 814 models when the number of studied precipitation events is expanded) that can learn the QPE  
 815 uncertainties conditional on time of day, weather, climate and geomorphological regimes for both  
 816 radar QPE analysis and forecasts, advancing the understanding and quantification of orographic  
 817 precipitation uncertainty at high resolution across global mountains.

818 **7. Appendix A**



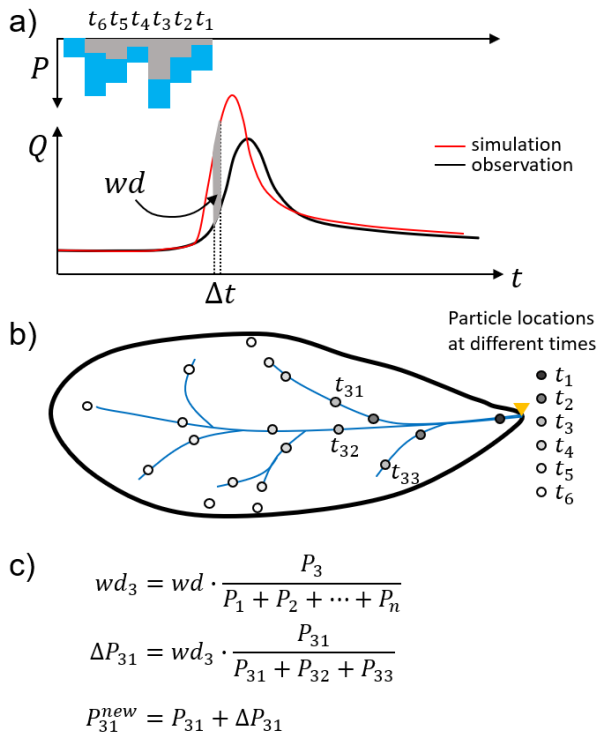
819 **Figure A1** - Spatial rainfall fields on 2014-05-15, 06-07 UTC. Rain rates between 0 to 1mm/h are  
 820 mapped in white.

Formatted: Font: Bold

822

823 The detailed distribution process of water difference (wd) is illustrated in Figure A2+ following  
 824 Section 2.3.8.

825



826

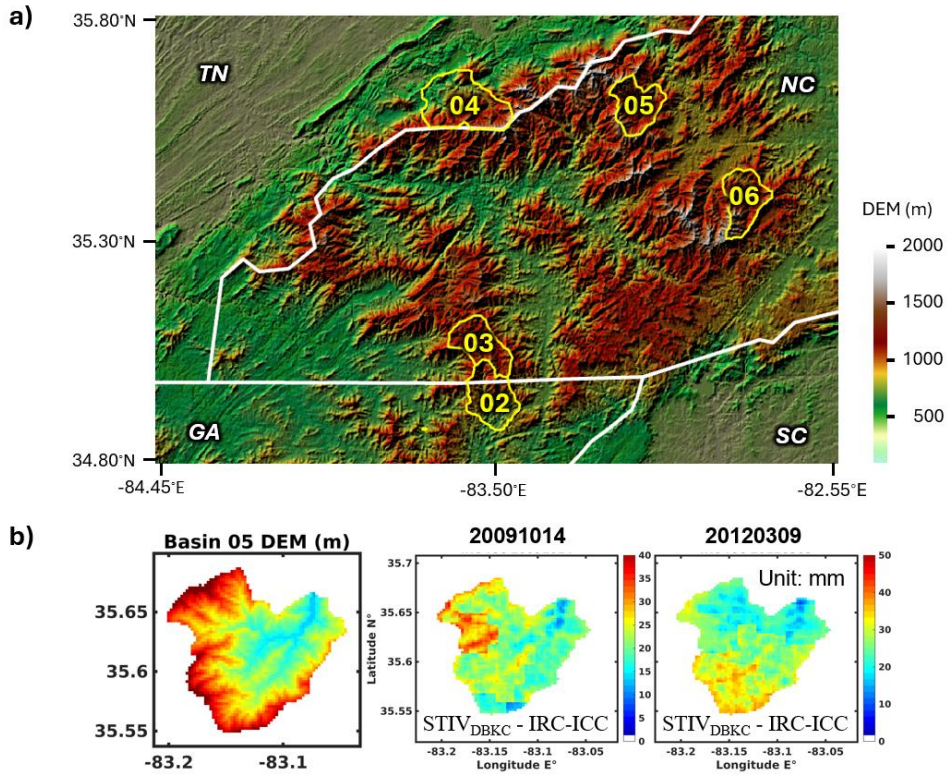
827 **Figure A1-A2** - Schematic depiction of the IRC framework and key mathematical equations. Panel  
 828 (a) illustrates the nonlinear relationship between streamflow and precipitation, where  $wd$   
 829 represents the residual between discharge simulations and observations at the basin outlet. The  
 830 variation of precipitation in the basin as a function of time is shown by the basin hyetograph in  
 831 blue. The hyetograph time series (blue) spans the duration of the precipitation event between  $t_1$   
 832 to  $t_n$ . In gray is the hyetograph over the area of interest for panels (b) and (c). To map the

833 streamlines, water particles are launched every time step and their trajectory to the outlet is tracked  
834 and saved. Panel **(b)** shows the source areas of water particles launched at various time steps  
835 ( $t_1, t_2, \dots t_6 \dots$ ) from all locations where runoff is produced, and the particles are tracked until they  
836 eventually reach the basin outlet. The streamlines of particles that reach the outlet at the same time  
837 are used to distribute the residuals backwards to the runoff source areas where the particles were  
838 originally launched (e.g., the three particles  $t_{31}, t_{32}$ , and  $t_{33}$  that reach the basin outlet at time  $t_3$ ).  
839 Panel **(c)** shows the algorithm to calculate the rainfall bias correction at location  $t_{31}$  due to the  
840 residual  $wd_3$  at time  $t_3$ .  $P_i$  is basin averaged rainfall at time  $t_i$ , and  $wd_3$  is the runoff volume to  
841 be corrected at time step  $t_3$ .  $\Delta P_{31}$  is the precipitation correction for pixel  $t_{31}$ , and precipitation  
842 amount at pixel  $t_{31}$  before and after IRC are denoted by  $P_{31}$  and  $P_{31}^{new}$ . This figure is adapted from  
843 Liao and Barros (2025b).

844

845 A zoom in map of the Southern Appalachians is plotted associated with DEM maps of other basins.  
846 A complete set of maps for each individual basin can be requested. Note, the rain gauges used in  
847 this study are plotted in Figure 1, and they are primarily near Basin05.

848



849

850 **Figure A32** – A zoom-in map of the Figure 4 for watersheds in the Southern Appalachians (Panel  
851 a). The DEM map and examples of rainfall event accumulation of Basin 05 (Panel b) to show  
852 rainfall alignment with topography.

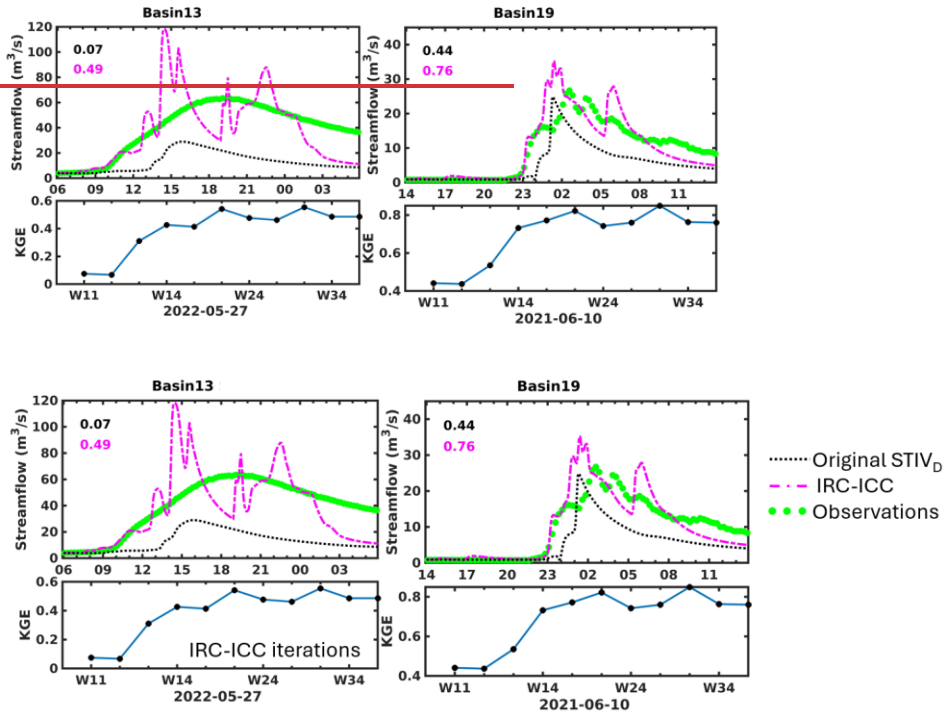
853

854

855

856

857



858

859 **Figure A43** – Examples of the coupled IRC-ICC framework application in Basin 13 and Basin 19  
860 for discussion in the manuscript. KGE values are displayed in the top left corners. Basin 13 is  
861 located in Karst terrain, while the event in Basin 19 is an example with a complex hydrograph.

862

863 **CREDIT AUTHOR STATEMENT**

864 M. Liao: Methodology, Data curation, Writing - original draft, Investigation. A. P. Barros:  
865 Conceptualization, Methodology, Writing - review & editing, Supervision, Project administration,  
866 Funding acquisition.

867 **COMPETING INTERESTS**

868 The authors declare there are no competing interests.

869 **ACKNOWLEDGMENTS**

870 The work was supported by NASA Earth System Science Fellowship associated with the first  
871 author and supported by a joint effort from NASA grant 80NSSC19K0685 and a grant from the  
872 IBM Accelerator program with the second author.

873

874 **REFERENCES**

- 875 Alimonti, G., Mariani, L., Prodi, F., & Ricci, R. A. (2022). A critical assessment of extreme  
876 events trends in times of global warming. *European Physical Journal - Plus*, 137, 112.  
877 <https://doi.org/10.1140/epjp/s13360-021-02243-9>
- 878 Allen, J. T. (2018). Climate change and severe thunderstorms. In Oxford research encyclopedia  
879 of climate science. <https://doi.org/10.1093/acrefore/9780190228620.013.62>
- 880 Andrieu, H., Creutin, J. D., Delrieu, G., & Faure, D. (1997). Use of a weather radar for the  
881 hydrology of a mountainous area. Part I: Radar measurement interpretation. *Journal of*  
882 *Hydrology*, 193(1-4), 1-25.
- 883 Areerachakul, N., Prongnuch, S., Longsomboon, P., & Kandasamy, J. (2022). Quantitative  
884 precipitation estimation (QPE) rainfall from meteorology radar over Chi Basin. *Hydrology*,  
885 9(10), 178. <https://doi.org/10.3390/hydrology9100178>
- 886 Arulraj, M., & Barros, A. P. (2017). Shallow precipitation detection and classification using  
887 multifrequency radar observations and model simulations. *Journal of Atmospheric and Oceanic*  
888 *Technology*, 34(9), 1963-1983. <https://doi.org/10.1175/JTECH-D-17-0060.1>
- 889 Arulraj, M., & Barros, A. P. (2021). Automatic detection and classification of low-level  
890 orographic precipitation processes from space-borne radars using machine learning. *Remote*  
891 *Sensing of Environment*, 257, 112355. <https://doi.org/10.1016/j.rse.2021.112355>
- 892 Barros, A., & Arulraj, M. (2020). Remote sensing of orographic precipitation. In V. Levizzani,  
893 C. Kidd, D. B. Kirschbaum, C. D. Kummerow, K. Nakamura, & F. J. Turk (Eds.), *Satellite*  
894 *precipitation measurement*. Springer. [https://doi.org/10.1007/978-3-030-35798-6\\_6](https://doi.org/10.1007/978-3-030-35798-6_6)
- 895 Barros, A., Miller, D., Wilson, A., Cutrell, G., Arulraj, M., Super, P., & Petersen, W. (2017).  
896 GPM Ground Validation Southern Appalachian Rain Gauge IPHEX [indicate subset used].  
897 Dataset available online from the NASA Global Hydrometeorology Resource Center DAAC,  
898 Huntsville, Alabama, U.S.A. DOI:  
899 <http://dx.doi.org/10.5067/GPMGV/IPHEX/GAUGES/DATA301>
- 900 Barros, A.P., Petersen, W., Schwaller, M., Cifelli, R., Mahoney, K., Peters-Liddard, C.,  
901 Shepherd, M., Nesbitt, S., Wolff, D., Heymsfield, G. & Starr, D. (2014) NASA GPM-Ground  
902 Validation: Integrated Precipitation and Hydrology Experiment 2014 Science Plan. EPL/Duke  
903 University: Durham, N.C. <https://doi.org/10.7924/G8CC0XMR>.
- 904 Berndt, C., Rabiei, E., & Haberlandt, U. (2014). Geostatistical merging of rain gauge and radar  
905 data for high temporal resolutions and various station density scenarios. *Journal of Hydrology*,  
906 508, 88-101. <https://doi.org/10.1016/j.jhydrol.2013.10.028>
- 907 Bindlish, R. and Barros, A.P., (1996): Aggregation of Digital Terrain Data Using a Modified  
908 Fractal Interpolation Scheme. *Computers & Geosciences*, 22, 907-917.
- 909 Bindlish, R., & Barros, A. P. (2000). Disaggregation of rainfall for one-way coupling of  
910 atmospheric and hydrological models in regions of complex terrain. *Global and Planetary*  
911 *Change*, 25(1-2), 111-132. [https://doi.org/10.1016/S0921-8181\(00\)00024-2](https://doi.org/10.1016/S0921-8181(00)00024-2)

912

Formatted: Italian (Italy)

Formatted: English (United States)

913 Bohling, G. (2005). Introduction to geostatistics and variogram analysis. Kansas geological  
914 survey, 1(10), 1-20.

915 Borga, M., Stoffel, M., Marchi, L., Marra, F., & Jakob, M. (2014). Hydrogeomorphic response to  
916 extreme rainfall in headwater systems: Flash floods and debris flows. *Journal of Hydrology*, 518,  
917 194-205.

918 Buytaert, W., Celleri, R., Willems, P., De Bievre, B., & Wyseure, G. (2006). Spatial and  
919 temporal rainfall variability in mountainous areas: A case study from the south Ecuadorian  
920 Andes. *Journal of hydrology*, 329(3-4), 413-421. <https://doi.org/10.1016/j.jhydrol.2006.02.031>

921 Carlson, D., (2010). Influence of lithology on vertical anisotropy of permeability at a field scale  
922 for select Louisiana geologic units. Gulf Coast Association of Geological Societies Transactions,  
923 60: 103-118.

924 Cassiraga, E., Gómez-Hernández, J. J., Berenguer, M., Sempere-Torres, D., & Rodrigo-Illarri, J.  
925 (2021). Spatiotemporal precipitation estimation from rain gauges and meteorological radar using  
926 geostatistics. *Mathematical Geosciences*, 53, 499-516. [https://doi.org/10.1007/s11004-020-](https://doi.org/10.1007/s11004-020-09882-1)  
927 [09882-1](https://doi.org/10.1007/s11004-020-09882-1),

928 Chen, J., Kumar, P., 2001. Topographic influence on the seasonal and interannual variation of  
929 water and energy balance of basins in North America. *Journal of Climate*, 14(9).

930 Czigány, S., Pirkhoffer, E., & Geresdi, I. (2010). Impact of extreme rainfall and soil moisture on  
931 flash flood generation. *Quarterly Journal of the Hungarian Meteorological Service*, 114(1-2),  
932 79-100.

933 Deijns, A. A., Dewitte, O., Thiery, W., d'Oreye, N., Malet, J. P., & Kervyn, F. (2022). Timing  
934 landslide and flash flood events from SAR satellite: a regionally applicable methodology  
935 illustrated in African cloud-covered tropical environments. *Natural Hazards and Earth System*  
936 *Sciences*, 22(11), 3679-3700. <https://doi.org/10.5194/nhess-22-3679-2022>

937 Delrieu, G., Wijbrans, A., Boudevillain, B., Faure, D., Bonnifait, L., & Kirstetter, P. E. (2014).  
938 Geostatistical radar-rain gauge merging: A novel method for the quantification of rain estimation  
939 accuracy. *Advances in Water Resources*, 71, 110-124.  
940 <https://doi.org/10.1016/j.advwatres.2014.06.005>

941 Diggle, P. and Ribeiro, P. J., 2007. Model-based geostatistics. Springer Series in Statistics, 230.

942 Dinku, T., Anagnostou, E. N., & Borga, M. (2002). Improving radar-based estimation of rainfall  
943 over complex terrain. *Journal of Applied Meteorology and Climatology*, 41(12), 1163-1178.  
944 [https://doi.org/10.1175/1520-0450\(2002\)041<1163:IRBEOR>2.0.CO;2](https://doi.org/10.1175/1520-0450(2002)041<1163:IRBEOR>2.0.CO;2)

945 Diomede, T., Davolio, S., Marsigli, C., Miglietta, M. M., Moscatello, A., Papetti, P., ... &  
946 Malguzzi, P. (2008). Discharge prediction based on multi-model precipitation forecasts.  
947 *Meteorology and atmospheric physics*, 101, 245-265. <https://doi.org/10.1007/s00703-007-0285-0>

948 Dobler, C., Hagemann, S., Wilby, R. L., & Stötter, J. (2012). Quantifying different sources of  
949 uncertainty in hydrological projections in an Alpine watershed. *Hydrology and Earth System*  
950 *Sciences*, 16(11), 4343-4360. <https://doi.org/10.5194/hess-16-4343-2012>

951 Duan, Y., Wilson, A.M., and Barros, A.P., 2015: Scoping a Field Experiment: Error Diagnostics  
952 of TRMM Precipitation Radar Estimates in Complex Terrain as a basis for IPHEX2014. *Hydrol.*  
953 *Earth Sys. Sci.*, 19,1501-1520.<https://doi.org/10.5194/hess-19-1501-2015>.

Formatted: English (United States)

Formatted: No underline, Font color: Auto, English (United States)

Formatted: English (United States)

Formatted: Portuguese (Brazil)

Formatted: Font: (Default) Times New Roman, 12 pt

Formatted: Font: (Default) Times New Roman, 12 pt

Formatted: Font: (Default) Times New Roman, 12 pt, No underline

Formatted: Font: (Default) Times New Roman, 12 pt

Formatted: Font: (Default) Times New Roman, 12 pt

954 Duan, Y., & Barros, A. P. (2017). Understanding how low-level clouds and fog modify the  
 955 diurnal cycle of orographic precipitation using in situ and satellite observations. *Remote*  
 956 *Sensing*, 9(9), 920. <https://doi.org/10.3390/rs9090920>

957 Durden, S. L., Haddad, Z. S., Kitiyakara, A., & Li, F. K. (1998). Effects of nonuniform beam  
 958 filling on rainfall retrieval for the TRMM precipitation radar. *Journal of Atmospheric and*  
 959 *Oceanic Technology*, 15(3), 635-646. [https://doi.org/10.1175/1520-0426\(1998\)015<0635:EONBFO>2.0.CO;2](https://doi.org/10.1175/1520-0426(1998)015<0635:EONBFO>2.0.CO;2)

961 Foresti, L., & Pozdnoukhov, A. (2012). Exploration of alpine orographic precipitation patterns  
 962 with radar image processing and clustering techniques. *Meteorological Applications*, 19(4), 407-  
 963 419. <https://doi.org/10.1002/met.272>

964 Freeze, R.A., Cherry, J.A., 1979. *Groundwater*. Englewood Cliffs, N.J. : Prentice-Hall.

965 Fulton, J., & Ostrowski, J. (1998). Measuring real-time streamflow using emerging technologies:  
 966 Radar, hydroacoustics, and the probability concept. *Journal of Hydrology*, 357(1-2), 1-10.  
 967 <https://doi.org/10.1016/j.jhydrol.2008.03.028>

968 Gentilucci, M., Bufalini, M., D'Aprile, F., Materazzi, M., & Pambianchi, G. (2021). Comparison  
 969 of data from rain gauges and the IMERG product to analyse precipitation in mountain areas of  
 970 central Italy. *ISPRS International Journal of Geo-Information*, 10(12), 795.  
 971 <https://doi.org/10.3390/ijgi10120795>

972 Goudenhoofd, E., & Delobbe, L. (2009). Evaluation of radar-gauge merging methods for  
 973 quantitative precipitation estimates. *Hydrology and Earth System Sciences*, 13(2), 195-203.  
 974 <https://doi.org/10.5194/hess-13-195-2009>

975 Grillakis, M. G., Koutroulis, A. G., Komma, J., Tsanis, I. K., Wagner, W., & Blöschl, G. (2016).  
 976 Initial soil moisture effects on flash flood generation—A comparison between basins of  
 977 contrasting hydro-climatic conditions. *Journal of Hydrology*, 541, 206-217.

978 Gupta, H. V., Kling, H., Yilmaz, K. K., & Martinez, G. F. (2009). Decomposition of the mean  
 979 squared error and NSE performance criteria: Implications for improving hydrological  
 980 modelling. *Journal of hydrology*, 377(1-2), 80-91. <https://doi.org/10.1016/j.jhydrol.2009.08.003>

981 Gupta, V., Nautiyal, H., Kumar, V., Jamir, I., & Tandon, R. S. (2016). Landslide hazards around  
 982 Uttarkashi township, Garhwal Himalaya, after the tragic flash flood in June 2013. *Natural*  
 983 *Hazards*, 80, 1689-1707. <https://doi.org/10.1007/s11069-015-2048-4>

984 Harrison, D. L., Driscoll, S. J., & Kitchen, M. (2000). Improving precipitation estimates from  
 985 weather radar using quality control and correction techniques. *Meteorological Applications*, 7(2),  
 986 135-144. <https://doi.org/10.1017/S1350482700001468>

987 Huffman, G. J., R. F. Adler, D. T. Bolvin, G. J. Gu, E. J. Nelkin, K. P. Bowman, Y. Hong, E. F.  
 988 Stocker, and D. B. Wolff (2007), The TRMM multisatellite precipitation analysis (TMPA):  
 989 Quasi-global, multiyear, combined-sensor precipitation estimates at fine scales, J.  
 990 *Hydrometeorol.*, 8(1), 38–55. <https://doi.org/10.1175/JHM560.1>

991 Iwasaki, K., Katsuyama, M., & Tani, M. (2020). Factors affecting dominant peak-flow runoff-  
 992 generation mechanisms among five neighbouring granitic headwater catchments. *Hydrological*  
 993 *Processes*, 34(5), 1154-1166. <https://doi.org/10.1002/hyp.13656>

Formatted: Portuguese (Brazil)

Formatted: English (United States)

Formatted: Italian (Italy)

Formatted: Italian (Italy)

Formatted: Italian (Italy)

Field Code Changed

Formatted: Italian (Italy)

Formatted: Italian (Italy)

Formatted: Portuguese (Brazil)

Formatted: Portuguese (Brazil)

Formatted: Portuguese (Brazil)

Field Code Changed

994 Kim, G., & Barros, A. P. (2001). Quantitative flood forecasting using multisensor data and  
 995 neural networks. *Journal of Hydrology*, 246(1-4), 45-62. [https://doi.org/10.1016/S0022-](https://doi.org/10.1016/S0022-1694(01)00353-5)  
 996 [1694\(01\)00353-5](https://doi.org/10.1016/S0022-1694(01)00353-5)

997 Kobold, M., & Sušelj, K. (2005). Precipitation forecasts and their uncertainty as input into  
 998 hydrological models. *Hydrology and Earth System Sciences*, 9(4), 322-332.  
 999 <https://doi.org/10.5194/hess-9-322-2005>

1000 Kochendorfer, J., Rasmussen, R., Wolff, M., Baker, B., Hall, M. E., Meyers, T., ... & Leeper, R.  
 1001 (2017). The quantification and correction of wind-induced precipitation measurement errors.  
 1002 *Hydrology and Earth System Sciences*, 21(4), 1973-1989. [https://doi.org/10.5194/hess-21-1973-](https://doi.org/10.5194/hess-21-1973-2017)  
 1003 [2017](https://doi.org/10.5194/hess-21-1973-2017)

1004 Komma, J., Reszler, C., Blöschl, G., & Haiden, T. (2007). Ensemble prediction of floods–  
 1005 catchment non-linearity and forecast probabilities. *Natural Hazards and Earth System Sciences*,  
 1006 7(4), 431-444.

1007 Konrad II, C. E. (1994). Moisture trajectories associated with heavy rainfall in the Appalachian  
 1008 region of the United States. *Physical Geography*, 15(3), 227-248.  
 1009 <https://doi.org/10.1080/02723646.1994.10642514>

1010 Kreklow, J., Tetzlaff, B., Burkhard, B., & Kuhnt, G. (2020). Radar-based precipitation  
 1011 climatology in Germany—developments, uncertainties and potentials. *Atmosphere*, 11(2), 217.  
 1012 <https://doi.org/10.3390/atmos11020217>

1013 Laiolo, P., Gabellani, S., Campo, L., Silvestro, F., Delogu, F., Rudari, R., ... & Puca, S. (2016).  
 1014 Impact of different satellite soil moisture products on the predictions of a continuous distributed  
 1015 hydrological model. *International Journal of Applied Earth Observation and Geoinformation*,  
 1016 48, 131-145. <https://doi.org/10.1016/j.jag.2015.06.002>

1017 Li, J., & Heap, A. D. 2008. A review of spatial interpolation methods for environmental  
 1018 scientists. 11-12.

1019 Liao, M., & Barros, A. P. (2019). The Integrated Precipitation and Hydrology Experiment-  
 1020 Hydrologic Applications for the Southeast US (IPHEX-H4SE) Part IV: High-Resolution  
 1021 Enhanced Stage IV-Rain gauge Combined Precipitation Product [Dataset]. Durham, NC: Duke  
 1022 Digital Repository. <https://idn.duke.edu/ark:/87924/r4pc2zd75>

1023 Liao, M., & Barros, A. P. (2022). Toward optimal rainfall – Hydrologic QPE correction in  
 1024 headwater basins. *Remote Sensing of Environment*, 279, 113107.  
 1025 <https://doi.org/10.1016/j.rse.2022.113107>

1026 Liao, M., & Barros, A.P., (2025a). Model Celerity-Discharge Behavior in Complex Terrain to  
 1027 Improve Orographic Quantitative Precipitation Estimation and Hydrologic Prediction in  
 1028 Headwater Basins. *Water Resources Research*, <https://doi.org/10.1029/2024WR038446>

1029 Liao, M., & Barros, A.P., (2025b). Toward optimal rainfall – Hydrologic QPE Correction in  
 1030 Headwater Basins — Closing the Water Budget within Observational Uncertainty Through  
 1031 Correcting Initial Soil Moisture Conditions. *J. Hydrology-Reg. Studies*,  
 1032 <https://doi.org/10.1016/j.ejrh.2025.102700>.

1033 Liao, M., & Barros, A. (2025c). StageIV-IRC – A High-resolution Dataset of Extreme  
 1034 Orographic Quantitative Precipitation Estimates (QPE) Constrained to Water Budget Closure for

Formatted: Italian (Italy)

Formatted: Italian (Italy)

Formatted: Italian (Italy)

Field Code Changed

Formatted: Portuguese (Brazil)

Formatted: Portuguese (Brazil)

Formatted: Portuguese (Brazil)

Field Code Changed

Formatted: English (United States)

Formatted: English (United States)

- 1035 Historical Floods in the Appalachian Mountains [Data set]. Zenodo.  
 1036 <https://doi.org/10.5281/zenodo.14028866>
- 1037
- 1038 Lin, Y., & Mitchell, K. E. (2005), The NCEP stage II/IV hourly precipitation analyses:  
 1039 Development and applications, paper presented at 19th Conference on Hydrology [Dataset], Am.  
 1040 Meteorol. Soc., San Diego, Calif., 9–13 Jan.
- 1041 Linsley, R.K., Kohler, J., Max A., Paulhus, J.L.H., (1982). Hydrology for Engineers. Water  
 1042 Resources and Environmental Engineering. McGraw-Hill, New York.
- 1043 Lumbroso, D., & Gaume, E. (2012). Reducing the uncertainty in indirect estimates of extreme  
 1044 flash flood discharges. *Journal of hydrology*, 414, 16-30.
- 1045 Maggioni, V., & Massari, C. (2018). On the performance of satellite precipitation products in  
 1046 riverine flood modeling: A review. *Journal of hydrology*, 558, 214-224.
- 1047 Marchi, L., Borga, M., Preciso, E., & Gaume, E. (2010). Characterisation of selected extreme  
 1048 flash floods in Europe and implications for flood risk management. *Journal of Hydrology*, 394(1-  
 1049 2), 118-133.
- 1050 McBratney, A. B., & Webster, R. (1986). Choosing functions for semi-variograms of soil  
 1051 properties and fitting them to sampling estimates. *Journal of soil Science*, 37(4), 617-639.
- 1052 McBride, J. L., & Ebert, E. E. (2000). Verification of quantitative precipitation forecasts from  
 1053 operational numerical weather prediction models over Australia. *Weather and Forecasting*,  
 1054 15(1), 103-121.
- 1055 McKee, J. L., & Binns, A. D. (2016). A review of gauge–radar merging methods for quantitative  
 1056 precipitation estimation in hydrology. Canadian Water Resources Journal/Revue canadienne des  
 1057 ressources hydriques, 41(1-2), 186-203. <https://doi.org/10.1080/07011784.2015.1064786>
- 1058 Milly, P. C. D., Wetherald, R. T., Dunne, K. A., & Delworth, T. L. (2002). Increasing risk of  
 1059 great floods in a changing climate. *Nature*, 415(6871), 514-517. <https://doi.org/10.1038/415514a>
- 1060 Mockler, E. M., Chun, K. P., Sapriza-Azuri, G., Bruen, M., & Wheeler, H. S. (2016). Assessing  
 1061 the relative importance of parameter and forcing uncertainty and their interactions in conceptual  
 1062 hydrological model simulations. *Advances in Water Resources*, 97, 299-313.  
 1063 <https://doi.org/10.1016/j.advwatres.2016.10.008>
- 1064 Mtibaa, S., & Asano, S. (2022). Hydrological evaluation of radar and satellite gauge-merged  
 1065 precipitation datasets using the SWAT model: Case of the Terauchi catchment in Japan. *Journal*  
 1066 *of Hydrology: Regional Studies*, 42, 101134. <https://doi.org/10.1016/j.ejrh.2022.101134>
- 1067 Nanding, N., Rico-Ramirez, M. A., & Han, D. (2015). Comparison of different radar-rain gauge  
 1068 rainfall merging techniques. *Journal of Hydroinformatics*, 17(3), 422-445.  
 1069 <https://doi.org/10.2166/hydro.2015.001>
- 1070 Nogueira, M., and Barros, A.P., (2015): Transient Stochastic Downscaling of Quantitative  
 1071 Precipitation Estimates for Hydrological Applications. *J. Hydrology*, No. 529, 1407- [1421](https://doi.org/10.1016/j.jhydrol.2015.08.041).  
 1072 <https://doi.org/10.1016/j.jhydrol.2015.08.041>.
- 1073 Oliver, M. A., & Webster, R. (2015). *Basic steps in geostatistics: the variogram and kriging*  
 1074 (Vol. 106). Cham, Switzerland: Springer International Publishing.

Field Code Changed

- 1075 Penna, D., Tromp-van Meerveld, H. J., Gobbi, A., Borga, M., & Dalla Fontana, G. (2011). The  
 1076 influence of soil moisture on threshold runoff generation processes in an alpine headwater  
 1077 catchment. *Hydrology and Earth System Sciences*, 15(3), 689-702. [https://doi.org/10.5194/hess-](https://doi.org/10.5194/hess-15-689-2011)  
 1078 [15-689-2011](https://doi.org/10.5194/hess-15-689-2011)
- 1079 Pielke, R. A., & Downton, M. W. (2000). Precipitation and damaging floods: Trends in the  
 1080 United States, 1932–97. *Journal of climate*, 13(20), 3625-3637. [https://doi.org/10.1175/1520-](https://doi.org/10.1175/1520-0442(2000)013<3625:PADFTI>2.0.CO;2)  
 1081 [0442\(2000\)013<3625:PADFTI>2.0.CO;2](https://doi.org/10.1175/1520-0442(2000)013<3625:PADFTI>2.0.CO;2)
- 1082 Prat, O. P., & Barros, A. P. (2010a). Assessing satellite-based precipitation estimates in the  
 1083 Southern Appalachian mountains using rain gauges and TRMM PR. *Advances in*  
 1084 *Geosciences*, 25, 143-153. <https://doi.org/10.5194/adgeo-25-143-2010>
- 1085 Prat, O. P., & Barros, A. P. (2010b). Ground observations to characterize the spatial gradients  
 1086 and vertical structure of orographic precipitation—Experiments in the inner region of the Great  
 1087 Smoky Mountains. *Journal of Hydrology*, 391(1-2), 141-156.  
 1088 <https://doi.org/10.1016/j.jhydrol.2010.07.013>
- 1089 Rafieenasab, A., Norouzi, A., Seo, D. J., & Nelson, B. (2015). Improving high-resolution  
 1090 quantitative precipitation estimation via fusion of multiple radar-based precipitation products.  
 1091 *Journal of Hydrology*, 531, 320-336. <https://doi.org/10.1016/j.jhydrol.2015.04.066>
- 1092 Schiemann, R., Erdin, R., Willi, M., Frei, C., Berenguer, M., & Sempere-Torres, D. (2011).  
 1093 Geostatistical radar-rain gauge combination with nonparametric correlograms: methodological  
 1094 considerations and application in Switzerland. *Hydrology and Earth System Sciences*, 15(5),  
 1095 1515-1536. <https://doi.org/10.5194/hess-15-1515-2011>
- 1096 Schumacher, R. S. (2017). Heavy rainfall and flash flooding. In *Oxford research encyclopedia of*  
 1097 *natural hazard science*. <https://doi.org/10.1093/acrefore/9780199389407.013.132>
- 1098 Shao, Y., Fu, A., Zhao, J., Xu, J., & Wu, J. (2021). Improving quantitative precipitation  
 1099 estimates by radar-rain gauge merging and an integration algorithm in the Yishu River  
 1100 catchment, China. *Theoretical and Applied Climatology*, 144, 611-623.  
 1101 <https://doi.org/10.1007/s00704-021-03526-y>
- 1102 Sideris, I. V., Gabella, M., Erdin, R., & Germann, U. (2013). Real-time radar–rain-gauge  
 1103 merging using spatio-temporal co-kriging with external drift in the alpine terrain of Switzerland.  
 1104 *Quarterly Journal of the Royal Meteorological Society*, 140(680), 1097-1111.  
 1105 <https://doi.org/10.1002/qj.2188>
- 1106 Silvestro, F., Rossi, L., Campo, L., Parodi, A., Fiori, E., Rudari, R., & Ferraris, L. (2019).  
 1107 Impact-based flash-flood forecasting system: Sensitivity to high resolution numerical weather  
 1108 prediction systems and soil moisture. *Journal of Hydrology*, 572, 388-402.  
 1109 <https://doi.org/10.1016/j.jhydrol.2019.02.055>
- 1110 Smith, J. A., Baeck, M. L., Ntelekos, A. A., Villarini, G., & Steiner, M. (2011). Extreme rainfall  
 1111 and flooding from orographic thunderstorms in the central Appalachians. *Water Resources*  
 1112 *Research*, 47(4). <https://doi.org/10.1029/2010WR010190>
- 1113 Špitalar, M., Gourley, J. J., Lutoff, C., Kirstetter, P. E., Brilly, M., & Carr, N. (2014). Analysis of  
 1114 flash flood parameters and human impacts in the US from 2006 to 2012. *Journal of hydrology*,  
 1115 519, 863-870. Tao, K., and Barros, A.P., 2010: Fractal Downscaling of Satellite Precipitation

Formatted: Italian (Italy)

Formatted: Italian (Italy)

Formatted: Italian (Italy)

1116 Products for Hydrometeorological Applications. *J. Atmos. Oceanic Technol.*, 27 (3), 409-427.  
 1117 <https://doi.org/10.1175/2009JTECHA1219.1>

1118 [Tao, K., & Barros, A. P. \(2010\). Using fractal downscaling of satellite precipitation products for](#)  
 1119 [hydrometeorological applications. \*Journal of Atmospheric and Oceanic Technology\*, 27\(3\), 409-](#)  
 1120 [427.](#)

1121 [Tao, J., & Barros, A. P. \(2013\). Prospects for flash flood forecasting in mountainous regions—An](#)  
 1122 [investigation of Tropical Storm Fay in the Southern Appalachians. \*Journal of Hydrology\*, 506,](#)  
 1123 [69-89. <https://doi.org/10.1016/j.jhydrol.2013.02.052>](#)

1124 Tao, J., & Barros, A. P. (2014). Coupled prediction of flood response and debris flow initiation  
 1125 during warm-and cold-season events in the Southern Appalachians, USA. *Hydrology and Earth*  
 1126 *System Sciences*, 18(1), 367-388. <https://doi.org/10.5194/hess-18-367-2014>

1127 Tao, J., Wu, D., Gourley, J., Zhang, S. Q., Crow, W., Peters-Lidard, C., & Barros, A. P. (2016).  
 1128 Operational hydrological forecasting during the IPHEX-IOP campaign—Meet the  
 1129 challenge. *Journal of hydrology*, 541, 434-456. <https://doi.org/10.1016/j.jhydrol.2016.02.019>

1130 Tao, J., & Barros, A. P. (2018). Multi-year atmospheric forcing datasets for hydrologic modeling  
 1131 in regions of complex terrain—Methodology and evaluation over the Integrated Precipitation and  
 1132 Hydrology Experiment 2014 domain. *Journal of Hydrology*, 567, 824-842.  
 1133 <https://doi.org/10.1016/j.jhydrol.2016.12.058>

1134 Tao, J., and Barros, A.P., 2019: Multi-Year Surface Radiative Properties and Vegetation  
 1135 Parameters for Hydrologic Modeling in Regions of Complex Terrain – Methodology and  
 1136 Evaluation over the IPHEX2014 Domain. *J. Hydrology-Reg. Studies*, 22, e100596. <https://doi.org/10.1016/j.ejrh.2019.100596>.

1138 Troch, P. A., Smith, J. A., Wood, E. F., & de Troch, F. P. (1994). Hydrologic controls of large  
 1139 floods in a small basin: central Appalachian case study. *Journal of Hydrology*, 156(1-4), 285-  
 1140 309. [https://doi.org/10.1016/0022-1694\(94\)90082-5](https://doi.org/10.1016/0022-1694(94)90082-5)

1141 Uber, M., Vandervaere, J. P., Zin, I., Braud, I., Heistermann, M., Legouët, C., ... & Nord, G.  
 1142 (2018). How does initial soil moisture influence the hydrological response? A case study from  
 1143 southern France. *Hydrology and Earth System Sciences*, 22(12), 6127-6146.  
 1144 <https://doi.org/10.5194/hess-22-6127-2018>

1145 Vignal, B., Galli, G., Joss, J., & Germann, U. (2000). Three methods to determine profiles of  
 1146 reflectivity from volumetric radar data to correct precipitation estimates. *Journal of Applied*  
 1147 *Meteorology and Climatology*, 39(10), 1715-1726. [https://doi.org/10.1175/1520-0450-](https://doi.org/10.1175/1520-0450-39.10.1715)  
 1148 [39.10.1715](#)

1149 Villarini, G., & Krajewski, W. F. (2010). Review of the different sources of uncertainty in single  
 1150 polarization radar-based estimates of rainfall. *Surveys in geophysics*, 31, 107-129.  
 1151 <https://doi.org/10.1007/s10712-009-9079-x>

1152 Vivoni, E. R., Entekhabi, D., Bras, R. L., & Ivanov, V. Y. (2007). Controls on runoff generation  
 1153 and scale-dependence in a distributed hydrologic model. *Hydrology and Earth System Sciences*,  
 1154 11(5), 1683-1701. <https://doi.org/10.5194/hess-11-1683-2007>

Formatted: Font: (Default) Times New Roman, 12 pt

Formatted: Space After: 8 pt, Line spacing: Multiple 1.16 li

Formatted: Font color: Auto, English (United States), Pattern: Clear

Formatted: English (United States)

- 1155 Wang, K. H., Chu, T., Yang, M. D., & Chen, M. C. (2020). Geostatistical based models for the  
 1156 spatial adjustment of radar rainfall data in typhoon events at a high-elevation river watershed.  
 1157 *Remote Sensing*, 12(9), 1427. <https://doi.org/10.3390/rs12091427>
- 1158 Wang, J., & Wolff, D. B. (2010). Evaluation of TRMM ground-validation radar-rain errors using  
 1159 rain gauge measurements. *Journal of Applied Meteorology and Climatology*, 49(2), 310-324.
- 1160 Weiland, F. C. S., Vrugt, J. A., Weerts, A. H., & Bierkens, M. F. (2015). Significant uncertainty  
 1161 in global scale hydrological modeling from precipitation data errors. *Journal of Hydrology*, 529,  
 1162 1095-1115. <https://doi.org/10.1016/j.jhydrol.2015.08.061>
- 1163 Wehbe, Y., Temimi, M., & Adler, R. F. (2020). Enhancing precipitation estimates through the  
 1164 fusion of weather radar, satellite retrievals, and surface parameters. *Remote Sensing*, 12(8), 1342.  
 1165 <https://doi.org/10.3390/rs12081342>
- 1166 Wernberg, T., Smale, D., Tuya, F., Thomsen, M. S., Langlois, T. J., de Bettignies, T., Bennett,  
 1167 S., & Rousseaux, C. S. (2013). An extreme climatic event alters marine ecosystem structure in a  
 1168 global biodiversity hotspot. *Nature Climate Change*, 3, 78–82.  
 1169 <https://doi.org/10.1038/nclimate1627>
- 1170 Wilson, A. M., & Barros, A. P. (2014). An investigation of warm rainfall microphysics in the  
 1171 southern Appalachians: Orographic enhancement via low-level seeder–feeder  
 1172 interactions. *Journal of the Atmospheric Sciences*, 71(5), 1783-1805.  
 1173 <https://doi.org/10.1175/JAS-D-13-0228.1>
- 1174 Wolvin, S., Strong, C., Rupper, S., & Steenburgh, W. J. (2024). Climatology of orographic  
 1175 precipitation gradients over High Mountain Asia derived from dynamical downscaling. *Journal*  
 1176 *of Geophysical Research: Atmospheres*, 129(20), e2024JD041010.  
 1177 <https://doi.org/10.1029/2024JD041010>
- 1178 Yildiz, O., & Barros, A. P. (2004). Climate variability, water resources, and hydrologic  
 1179 extremes—Modeling the water and energy budgets. In *Climate and Hydrology in Mountain*  
 1180 *Areas*, (Eds. C. de Jong, D. Collins, and R. Ranzi), John Wiley and Sons (Pub.), 303-318.  
 1181 <https://doi.org/10.1002/0470858249.ch20>
- 1182 Yildiz, O., & Barros, A. P. (2007). Elucidating vegetation controls on the hydroclimatology of a  
 1183 mid-latitude basin. *Journal of Hydrology*, 333(2-4), 431-448.  
 1184 <https://doi.org/10.1016/j.jhydrol.2006.09.010>
- 1185 Yıldız, O., & Barros, A. P. (2009). Evaluating spatial variability and scale effects on hydrologic  
 1186 processes in a midsize river basin. *Sci. Res. Essays*, 4, 217-225.  
 1187 <https://doi.org/10.5897/SRE.9000465>
- 1188 Zappa, M., Jaun, S., Germann, U., Walser, A., & Fundel, F. (2011). Superposition of three  
 1189 sources of uncertainties in operational flood forecasting chains. *Atmospheric Research*, 100(2-3),  
 1190 246-262. <https://doi.org/10.1016/j.atmosres.2010.12.005>
- 1191 Zehe, E., & Blöschl, G. (2004). Predictability of hydrologic response at the plot and catchment  
 1192 scales: Role of initial conditions. *Water Resources Research*, 40(10).
- 1193 Zhang, J., Howard, K., Langston, C., Kaney, B., Qi, Y., Tang, L., Grams, H., Wang, Y., Cocks,  
 1194 S., Martinaitis, S., Arthur, A., Cooper, K., Brogden, J., & Kitzmiller, D. (2016). Multi-radar  
 1195 multi-sensor (MRMS) quantitative precipitation estimation: Initial operating capabilities

Formatted: Portuguese (Brazil)

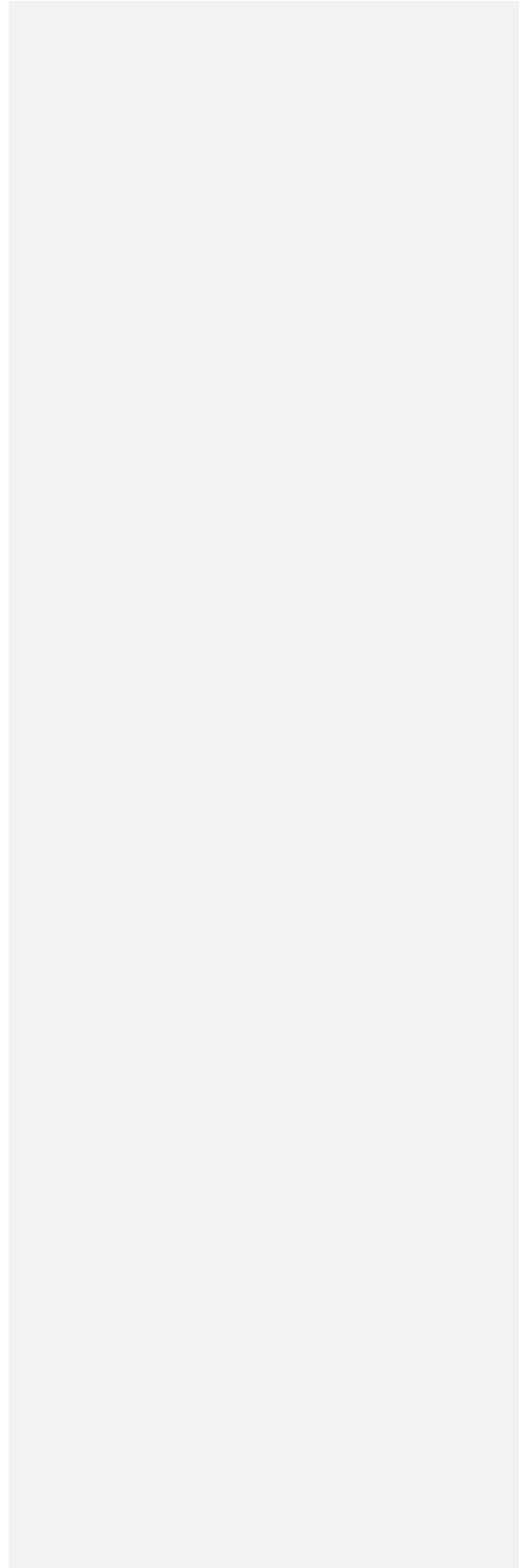
1196 [Dataset]. *Bulletin of the American Meteorological Society*, 97(4), 621–638.  
1197 <https://doi.org/10.1175/BAMS-D-14-00174.1>

1198 Zhang, X., & Anagnostou, E. N. (2019). Evaluation of numerical weather model–based satellite  
1199 precipitation adjustment in tropical mountainous regions. *Journal of Hydrometeorology*, 20(3),  
1200 431–445. <https://doi.org/10.1175/JHM-D-18-0008.1>

1201 Zhang, Y., Schaap, M. G., & Zha, Y. (2018). A high-resolution global map of soil hydraulic  
1202 properties produced by a hierarchical parameterization of a physically based water retention  
1203 model. *Water Resources Research*, 54(12), 9774–9790. <https://doi.org/10.1029/2018WR023539>

1204 Zimmerman, D. L., & Zimmerman, M. B. (1991). A comparison of spatial semivariogram  
1205 estimators and corresponding ordinary kriging predictors. *Technometrics*, 33(1), 77–91.  
1206 <https://doi.org/10.1080/00401706.1991.10484771>

1207  
1208



1210 **LIST OF TABLES**

1211 **Table 1** - Raingauge index and exact locations as illustrated in Figure 1. Two rain gauges  
1212 highlighted in bold font are installed at Purchase Knob, a supersite in the inner mountain region.  
1213 Locations equipped with more than one raingauge (collocated) are shaded in grey color, and these  
1214 collocated raingauges generally differ in tipping sizes. This table is adapted from Liao and Barros  
1215 (2019).

1216 **Table 2** - Hydrologic skills used in this work.

1217 **Table 3** - Information table for selected basins and corresponding streamflow gauges used in this  
1218 work. This table is adapted from Liao and Barros (2025b). Basin 07 and Basin 12 are the smallest  
1219 and largest basins respectively and were removed from further analysis. Red-coded rows represent  
1220 basins located in Karst terrain, which are ~~were not included~~ ~~discarded from~~ ~~in the final published~~  
1221 data due to the lack of Karst ~~analysis~~ hydrology processes in the hydrology model and  
1222 consequently lesser performance of the IRC ~~in this work~~.  
1223

1224

1225

1226

1227 **Table 1** – Raingauge index and exact locations as illustrated in Figure 1. Two rain gauges  
 1228 highlighted in bold font are installed at Purchase Knob, a supersite in the inner mountain region.  
 1229 Locations equipped with more than one raingauge (collocated) are shaded in grey color, and these  
 1230 collocated raingauges generally differ in tipping sizes. This table is adapted from Liao and Barros  
 1231 (2019).

NO.	Site ID.	Latitude	Longitude	Elevation (m)
01	RG 001	35.398	-82.913	1156
02	RG 002	35.417	-82.971	1731
03	RG 003	35.384	-82.916	1609
04	RG 004	35.368	-82.990	1922
05	RG 005	35.408	-82.964	1520
06	RG 008	35.382	-82.973	1737
07	RG 010	35.456	-82.946	1478
08	RG 100	35.586	-83.072	1495
09	RG 100T	35.587	-83.064	1485
10	RG 101	35.575	-83.088	1520
11	RG 102	35.563	-83.103	1635
12	RG 103	35.553	-83.117	1688
13	RG 104	35.554	-83.088	1584
14	RG 106	35.432	-83.029	1210
15	RG 109	35.495	-83.040	1500
16	RG 110	35.548	-83.148	1563
17	RG 300	35.726	-83.216	1558
18	RG 301	35.705	-83.255	2003
19	RG 302	35.721	-83.246	1860
20	<b>RG 303PK</b>	<b>35.586</b>	<b>-83.072</b>	<b>1495</b>
21	<b>RG 303S</b>	<b>35.762</b>	<b>-83.162</b>	<b>1490</b>
22	RG 304	35.670	-83.182	1820
23	RG 305	35.691	-83.131	1630
24	RG 306	35.745	-83.171	1536
25	RG 307	35.651	-83.199	1624
26	RG 308	35.730	-83.182	1471
27	RG 309	35.682	-83.150	1604
28	RG 310	35.702	-83.122	1756
29	RG 311	35.765	-83.140	1036
30	RG 400	35.702	-83.122	1756
31	RG 401	35.651	-83.199	1624
32	RG 402	35.721	-83.246	1860
33	RG 403	35.517	-83.101	925
34	RG 407	35.517	-83.101	925

1232

1233

1234 **Table 2:** Hydrologic skills used in this work.

Notation	Information	Reference
KGE	Kling-Gupta efficiency	Eq. (19) /Gupta et al. (2009)
EV	Relative error in flood volume	Eq. (20)
EPT	Error in peak flow timing	Flood front timing differences
EPV	Relative Error in maximum flow rate	Eq. (21)

1235

1236 **Table 3** – Information table for initially selected basins and corresponding streamflow gauges used  
 1237 in this work. This table is adapted from Liao and Barros (2025b). Basin 07 and Basin 12 are the  
 1238 smallest and largest basins and were removed from further analysis. Red-coded rows represent  
 1239 basins located in Karst terrain, which were discarded from the final published data due to the lack  
 1240 of Karst analysis in this work.

Basin index	USGS Gauge ID	Drainage area (km <sup>2</sup> )	Basin highest elevation (m)	Basin relief (m)	Location
1	3544970	118.7	1442	847	GA
2	2178400	176.1	1629	1051	GA
3	3504000	149.9	1667	1032	NC
4	3497300	317.6	1999	1651	TN
5	3460000	148.1	1879	1174	NC
6	3456500	152.8	1873	1157	NC
<b>7</b>	<b>3450000</b>	<b>15.8</b>	<b>1934</b>	<b>1047</b>	<b>NC</b>
8	344894205	41.3	1995	1221	NC
9	3463300	134.3	1989	1425	NC
10	3400500	234.7	1257	1257	KY
11	3479000	283.3	1772	1216	NC
<b>12</b>	<b>3161000</b>	<b>611.8</b>	<b>1834</b>	<b>1009</b>	<b>NC</b>
13	3182700	447.3	1111	717	WV
14	2011460	194.4	1388	763	VA
15	1620500	54.5	1321	712	VA
16	3180500	426.8	1416	621	WV
17	3068800	437.1	1471	908	WV
18	1595000	234.8	1230	560	MD
19	1595300	130.3	1069	712	WV
20	1544500	445.9	765	457	PA
21	1422747	81.4	766	394	NY
22	1415000	106.8	1019	636	NY
23	1413398	152.8	1094	754	NY
24	13621955	41.7	1074	717	NY
25	1421610	51.3	970	497	NY
26	1074520	389.4	1582	1582	NH
27	10642505	294.9	1895	1693	NH
28	1137500	300.3	1894	1546	NH
29	1133000	183.2	975	719	VT
30	1055000	334.1	1143	975	MAINE

Formatted: Font: Bold

Formatted: Font: Bold

Formatted Table

1241

1242

1243 **LIST OF FIGURES**

1244 **Figure 1** - Map of IPHEX (Barros et al., 2014) ground-based observations in the Southern  
1245 Appalachians. Raingauge is denoted as a character string starting with three-digit number  
1246 potentially followed by extra letters; locations started with a letter P represent disdrometers. The  
1247 basic information regarding these stations is listed in Table 1. This figure is adapted from Liao and  
1248 Barros (2019).

1249 **Figure 2** – Workflow to generate the product  $STIV_{DBKC}$ .

1250 **Figure 3** – An illustration of the structure of IRC, ICC and the coupled IRC-ICC framework  
1251 including **a)** the residual hydrograph between the observed and simulated discharge, with the  
1252 discharge water difference  $wd(t)$  being distributed across the time window  $T$ ; **b)** Example of travel  
1253 time distribution  $TT(t)$  and map (inset) illustrating a hypothetical distribution of runoff source  
1254 areas (in red,  $ns=3$ ) with travel time  $x_2$  contributing to streamflow at time  $t$ , meaning that at time  
1255  $t-x_2$  there are three pixels ( $ns=3$ ) generating runoff that reaches the outlet at time  $t$ .  $T$  is the time  
1256 window over which runoff source areas with  $TT < T$  are mapped and the inverse rainfall correction  
1257 (IRC) are applied; **c)** Example of IRC windows guided by timescales of dominant hydrological  
1258 processes. The first window solely covers the initial streamflow conditions before the target event.  
1259 The second window depicts the early rising limb of the hydrograph. The third window captures  
1260 the steep rising limb of the hydrograph until it reaches the peak flow. The fourth and fifth windows  
1261 correspond to interflow-dominant and baseflow-dominant stages of the recession curve  
1262 respectively, separated by the recession inflection point; **d)** A schematic drawing that shows  
1263 different characteristic timings in a hydrograph with the implementation of the Initial Condition  
1264 Correction (ICC) strategy. Specifically,  $T_r^*$  and  $T_r$  represent the timing of flood front in simulations  
1265 and observations, respectively.  $T_p$  is the timing of observed maximum flood. The inflection point  
1266 of the recession curve of the observations is denoted as  $T_i$ . Flow differences at  $t_1$  and  $t_2$  are denoted  
1267 as  $\Delta S_1$  and  $\Delta S_2$  respectively for the purpose of discussion.  $P$ ,  $Q$  and  $IC$  represent precipitation,  
1268 flow discharge and initial condition, respectively; **e)** The implemented framework in this work  
1269 consisting of ICC and IRC. This figure is adapted from Liao and Barros (2022, 2025b).

1270 **Figure 4** – Map of the Continental United States (CONUS) and headwater basins studied in this  
1271 work. Basin information is available in Table 3. Sub-regions are delineated as the following for  
1272 discussion purposes only: Northern, Central and Southern Appalachian Mountains (NAM, Basin  
1273 21-30; CAM, Basin 13-20; SAM, Basin 01-11). Basins 07 and 12, marked with red symbols, were  
1274 discarded due to basin size criteria. Basins 13 and 14 with blue symbols were discarded due to the  
1275 importance of karst hydrology processes that are not represented in the hydrology model used to  
1276 conduct the IRC. This figure is adapted from Liao and Barros (2025b). ~~Map of the Continental~~  
1277 ~~United States (CONUS) and headwater basins studied in this work. Basin information is available~~  
1278 ~~in Table 3. Sub-regions are delineated as the following for discussion purposes only: Northern,~~  
1279 ~~Central and Southern Appalachian Mountains (NAM, Basin 21-30; CAM, Basin 13-20; SAM,~~  
1280 ~~Basin 01-11). This figure is adapted from Liao and Barros (2025b).~~

1281 **Figure 5** - Examples of raingauge measurements showing the diurnal cycle of different seasons at  
1282 different locations: Left panel – raingauge RG008 located in the eastern ridges for the Summer  
1283 (JAS: July-August-September) season. Right panel – raingauge RG302 located in the western

1284 ridges for the Spring (AMJ; April-May-June) season. Rain gauge measurements (blue);  
1285 StageIV<sub>DBK</sub> (black); StageIV<sub>DBKC</sub> (green). This figure is from Liao and Barros (2019).

1286 **Figure 6** – Top row – The diurnal cycle of missing precipitation at RG003 (Eastern ridges) and  
1287 RG103 (Inner regions) for January-February-March (JFM) using various products. Bottom row-  
1288 corresponding rain gauge climatology (blue). StageIV<sub>D</sub> (black); StageIV<sub>DBK</sub> (cyan); StageIV<sub>DBKC</sub>  
1289 (green). This figure is from Liao and Barros (2019).

1290 **Figure 7** – Statistical evaluation summary for winter precipitation (JFM, January, February, and  
1291 March): a) Diurnal cycle of mean HSS and TS statistics including all rain gauges calculated using  
1292 all data from 2008 to 2017: STIV<sub>D</sub> (black) and STIV<sub>DBKC</sub> (green); b) HSS and TS statistics  
1293 calculated using different rain rate thresholds over the same 10-year period; c) Diurnal cycle of  
1294 rain rate RMSE at seasonal-scale, and its dependence on observed rainfall rate. This figure is from  
1295 Liao and Barros (2019).

1296 **Figure 8** – The IRC-ICC performance in Basin05 as an example for the 2017-10-23 event  
1297 (Basin05: Cataloochee Creek Basin, NC). This event is part of the 2017 Hurricane Nate. This  
1298 figure contains **a**) hydrological responses when precipitation forcing is the STIV<sub>DBKC</sub>. The dashed  
1299 rectangular plot consisting of intermediate results including each iteration from the IRC-ICC  
1300 framework (Figure 3). **b**) the hydrological equilibrium of the IRC-ICC after 5 iterations. This  
1301 figure is adapted from Liao and Barros (2025b).

1302 **Figure 9** – The IRC-ICC performance for different subregions, include **a**) 3 events from the  
1303 Southern Appalachians; **b**) 3 events from the Central Appalachians; and **c**) 3 events from the  
1304 Northern Appalachians. The IRC-ICC KGE evolution plots from iterations are included below the  
1305 hydrographs. The black and pink line are from the original STIV<sub>D</sub> and the IRC-ICC equilibrium  
1306 state (STIV<sub>D</sub><sup>IRC\*</sup>), respectively, and KGE values are displayed as colored numbers in the top left  
1307 corners. This figure is adapted from Liao and Barros (2025b).

1308 **Figure 10** – Event total precipitation maps for three cold season events (a) and three warm season  
1309 events (b). Each column represents one event, and each row represents one precipitation product:  
1310 STIV<sub>DBKC</sub>, STIV<sub>DBKC</sub><sup>IRC\*</sup> from IRC-only framework, and STIV<sub>DBKC</sub><sup>IRC\*</sup> from the coupled IRC-ICC  
1311 framework. This figure is adapted from Liao and Barros (2025b).

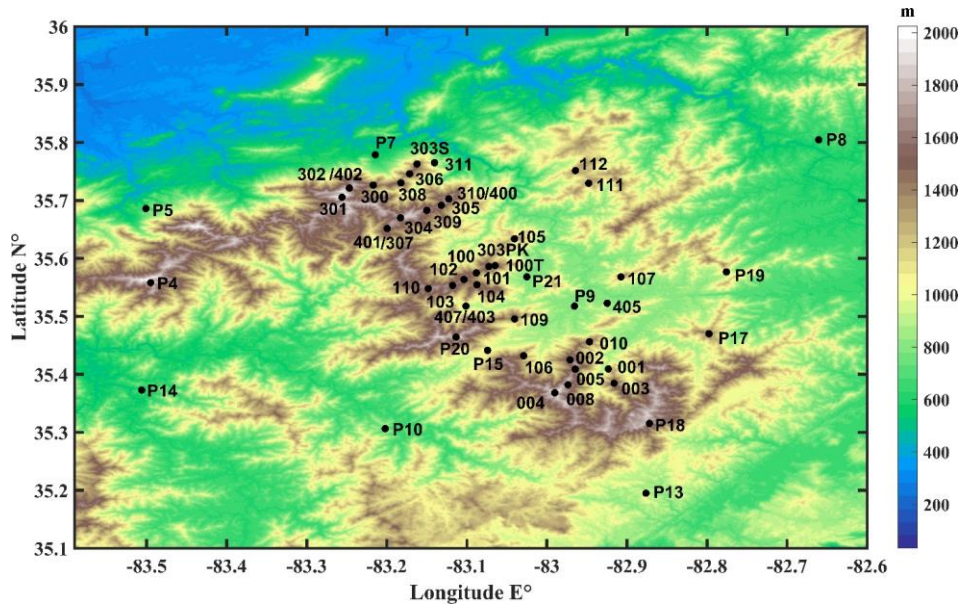
1312 **Figure 11** – Summary charts of precipitation statistics for all event-total precipitation maps. Basin  
1313 precipitation average and standard deviation for each event are represented by circles and triangles  
1314 in the top and bottom panel, respectively. Each panel consists of 3 sub-regions by vertical black  
1315 lines: the Southern Appalachian Mountains, Central Appalachian Mountains, and Northern  
1316 Appalachian Mountains. The list of events in Basin 05 (with event number ranging from 55 to  
1317 108) in the SAM is highlighted by a blue rectangle for further discussion in the text. The average  
1318 values of all events for both the mean and the standard deviation are calculated and shown in the  
1319 top right corner. Black color and pink color represent pre and post IRC-ICC QPE statistics,  
1320 respectively.

1321 **Figure 12** – Summary of hydrologic skills. Green dashed lines and associated uncertainty  
1322 envelopes are only for visual illustration. Hydrologic statistics are explained in Table 2. Pink and  
1323 black scatters (each scatter represent one event) represent IRC-ICC, and baseline outputs,  
1324 respectively. Each horizontal panel is split into 3 subsections by vertical black lines representing  
1325 the 3 subregions. Histograms graphs on the right hand side are provided for a summary view. This  
1326 figure is adapted from Liao and Barros (2025b).

1327 **Figure 13** – **a)** Event total QPE plots for various QPE datasets conditional on seasons and KGE  
1328 values; **b)** KGE distributions across events using different QPE datasets. This figure is adapted  
1329 from Liao and Barros (2025b).

1330

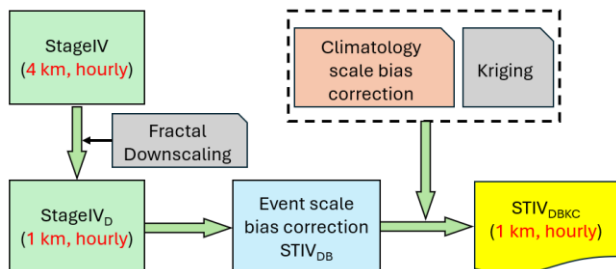
1331



1332

1333 **Figure 1** - Map of IPHEX (Barros et al., 2014) ground-based observations in the Southern  
1334 Appalachians. Rain gauge is denoted as a character string starting with three-digit number  
1335 potentially followed by extra letters; locations started with a letter P represent disdrometers. The  
1336 basic information regarding these stations is listed in Table 1. This figure is adapted from Liao and  
1337 Barros (2019).

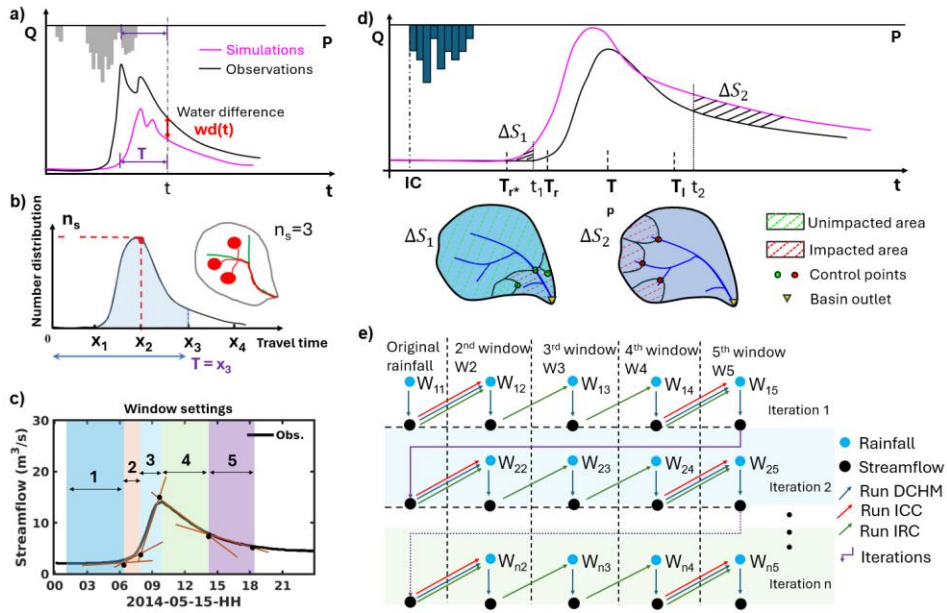
1338



1339

1340 **Figure 2** – Workflow to generate the product  $STIV_{DBKC}$ .

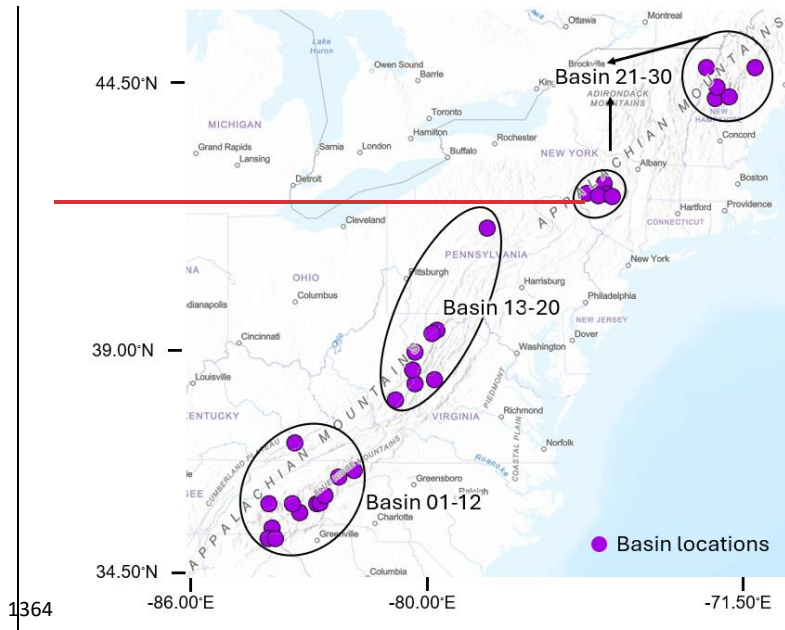
1341



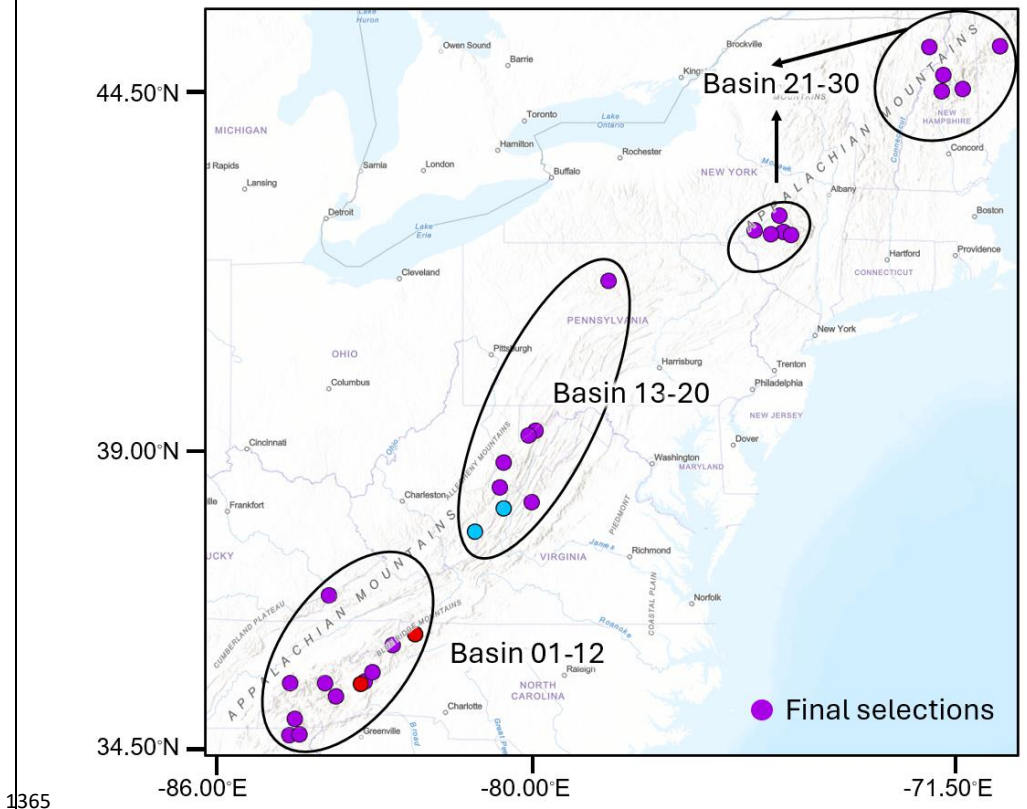
1342

1343 **Figure 3** – An illustration of the structure of IRC, ICC and the coupled IRC-ICC framework  
 1344 including **a)** the residual hydrograph between the observed and simulated discharge, with the  
 1345 discharge water difference  $wd(t)$  being distributed across the time window  $T$ ; **b)** Example of travel  
 1346 time distribution  $TT(t)$  and map (inset) illustrating a hypothetical distribution of runoff source  
 1347 areas (in red,  $n_s=3$ ) with travel time  $x_2$  contributing to streamflow at time  $t$ , meaning that at time  
 1348  $t-x_2$  there are three pixels ( $n_s=3$ ) generating runoff that reaches the outlet at time  $t$ .  $T$  is the time  
 1349 window over which runoff source areas with  $TT < T$  are mapped and the inverse rainfall correction  
 1350 (IRC) are applied; **c)** Example of IRC windows guided by timescales of dominant hydrological  
 1351 processes. The first window solely covers the initial streamflow conditions before the target event.  
 1352 The second window depicts the early rising limb of the hydrograph. The third window captures  
 1353 the steep rising limb of the hydrograph until it reaches the peak flow. The fourth and fifth windows  
 1354 correspond to interflow-dominant and baseflow-dominant stages of the recession curve  
 1355 respectively, separated by the recession inflection point; **d)** A schematic drawing that shows  
 1356 different characteristic timings in a hydrograph with the implementation of the Initial Condition  
 1357 Correction (ICC) strategy. Specifically,  $T_{r^*}$  and  $T_r$  represent the timing of flood front in simulations  
 1358 and observations, respectively.  $T_p$  is the timing of observed maximum flood. The inflection point  
 1359 of the recession curve of the observations is denoted as  $T_i$ . Flow differences at  $t_1$  and  $t_2$  are  
 1360 denoted as  $\Delta S_1$  and  $\Delta S_2$  respectively for the purpose of discussion.  $P$ ,  $Q$  and  $IC$  represent precipitation,  
 1361 flow discharge and initial condition, respectively; **e)** The implemented framework in this work  
 1362 consisting of ICC and IRC. This figure is adapted from Liao and Barros (2022, 2025b).

1363

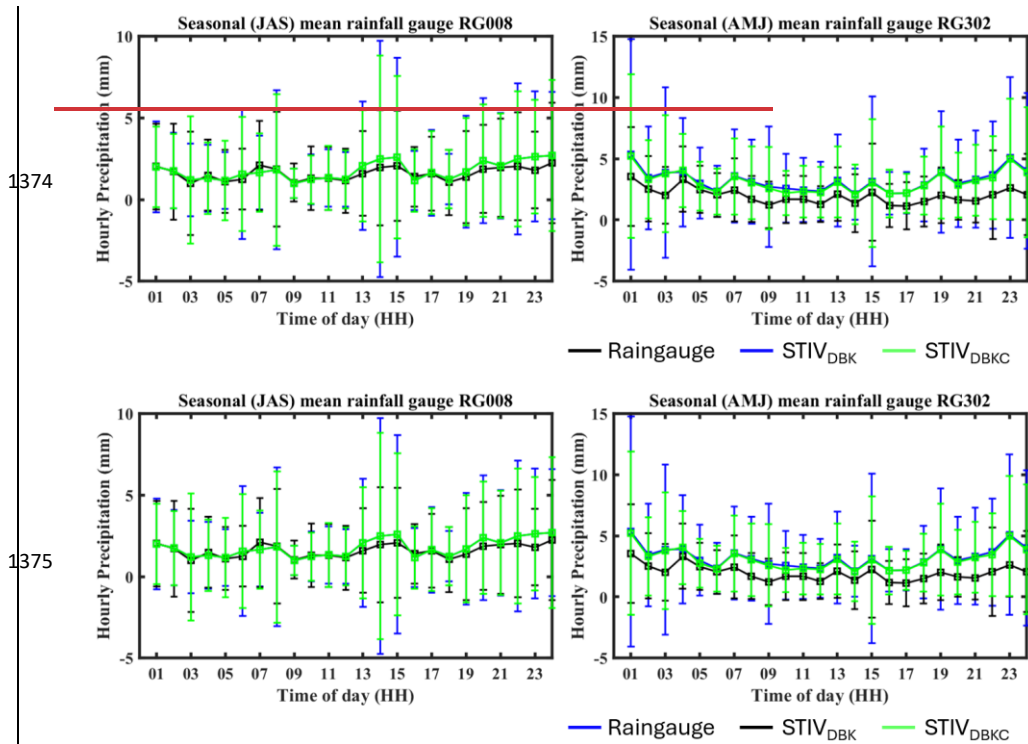


1364



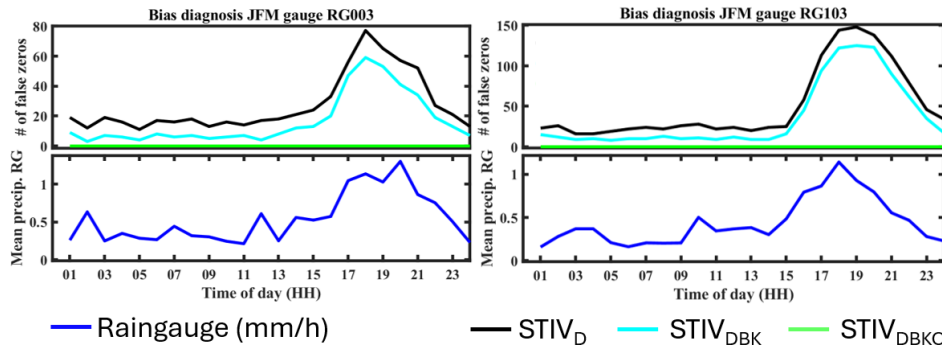
1366 **Figure 4** – Map of the Continental United States (CONUS) and headwater basins studied in this  
 1367 work. Basin information is available in Table 3. Sub-regions are delineated as the following for  
 1368 discussion purposes only: Northern, Central and Southern Appalachian Mountains (NAM, Basin  
 1369 21-30; CAM, Basin 13-20; SAM, Basin 01-11). Basins 07 and 12, marked with red symbols, were  
 1370 discarded due to basin size criteria. Basins 13 and 14 with blue symbols were discarded due to the  
 1371 importance of karst hydrology processes that are not represented in the hydrology model used to  
 1372 conduct the IRC. This figure is adapted from Liao and Barros (2025b).

1373



1376 **Figure 5** – Examples of raingauge measurements showing the diurnal cycle of different seasons  
 1377 at different locations: Left panel – raingauge RG008 located in the eastern ridges for the Summer  
 1378 (JAS: July-August-September) season. Right panel – raingauge RG302 located in the western  
 1379 ridges for the Spring (AMJ; April-May-June) season. Rain gauge measurements (blue);  
 1380 StageIV<sub>DBK</sub> (black); StageIV<sub>DBKc</sub> (green). This figure is from Liao and Barros (2019).

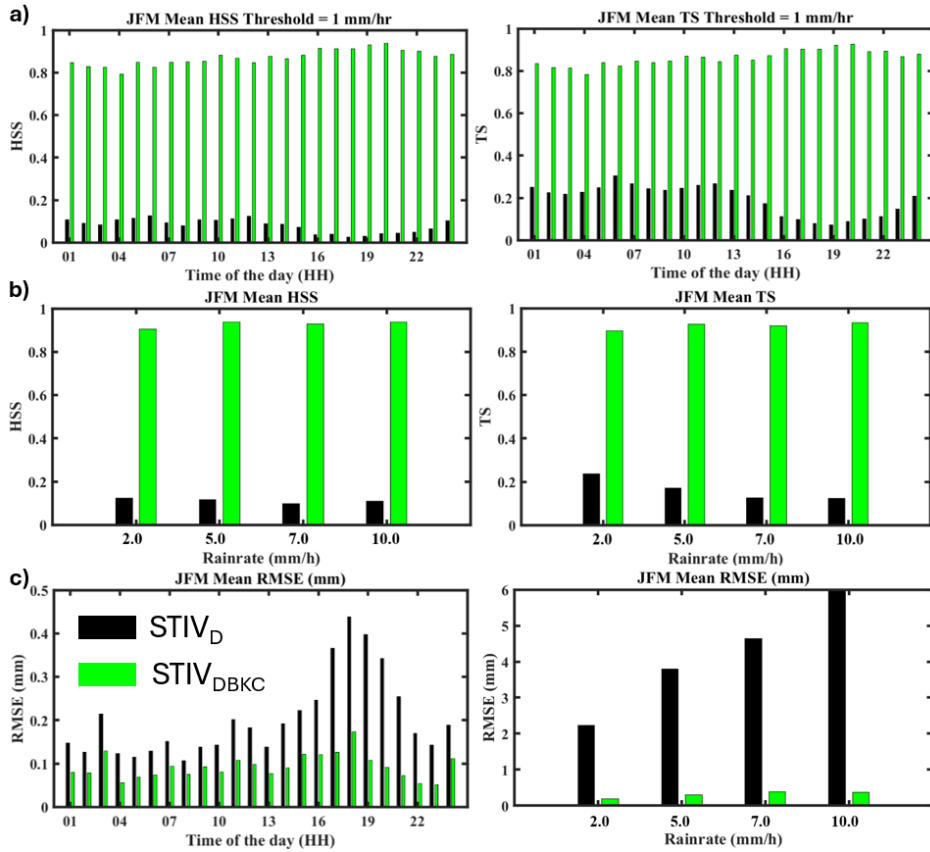
1381



1382

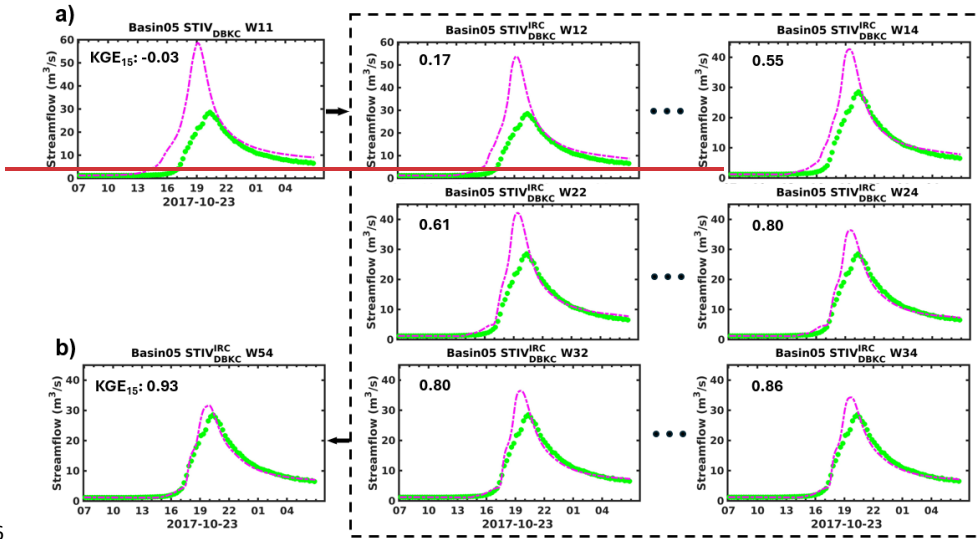
1383 **Figure 6** –Top row – The diurnal cycle of missing precipitation at RG003 (Eastern ridges) and  
 1384 RG103 (Inner regions) for January-February-March (JFM) using various products. Bottom row-  
 1385 corresponding rain gauge climatology (blue). StageIV<sub>D</sub> (black); StageIV<sub>DBK</sub> (cyan); StageIV<sub>DBKc</sub>  
 1386 (green). This figure is from Liao and Barros (2019).

1387

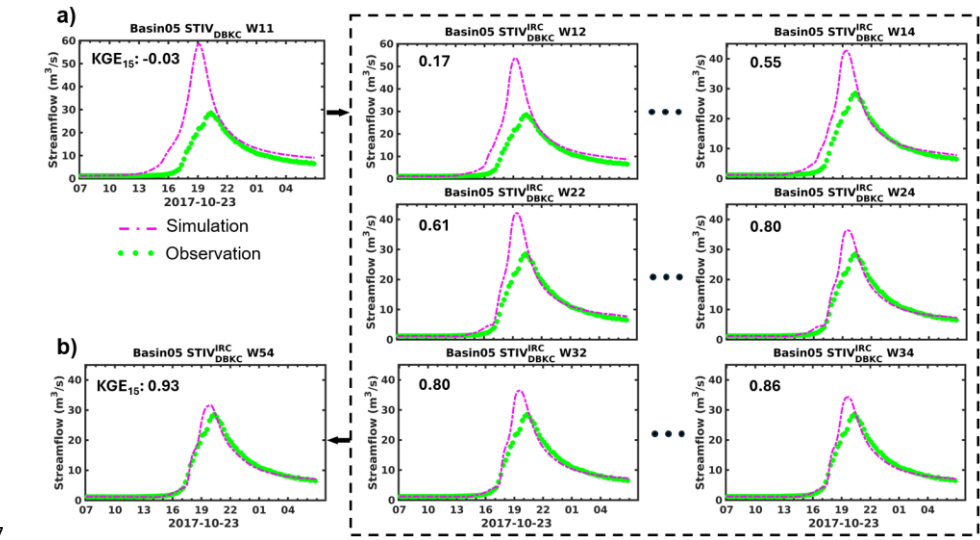


1390 **Figure 7** – Statistical evaluation summary for winter precipitation (JFM, January, February, and  
 1391 March): a) Diurnal cycle of mean HSS and TS statistics including all rain gauges calculated using  
 1392 all data from 2008 to 2017: STIV<sub>D</sub> (black) and STIV<sub>DBKC</sub> (green); b) HSS and TS statistics  
 1393 calculated using different rain rate thresholds over the same 10-year period; c) Diurnal cycle of  
 1394 rain rate RMSE at seasonal-scale, and its dependence on observed rainfall rate. This figure is from  
 1395 Liao and Barros (2019).

1396



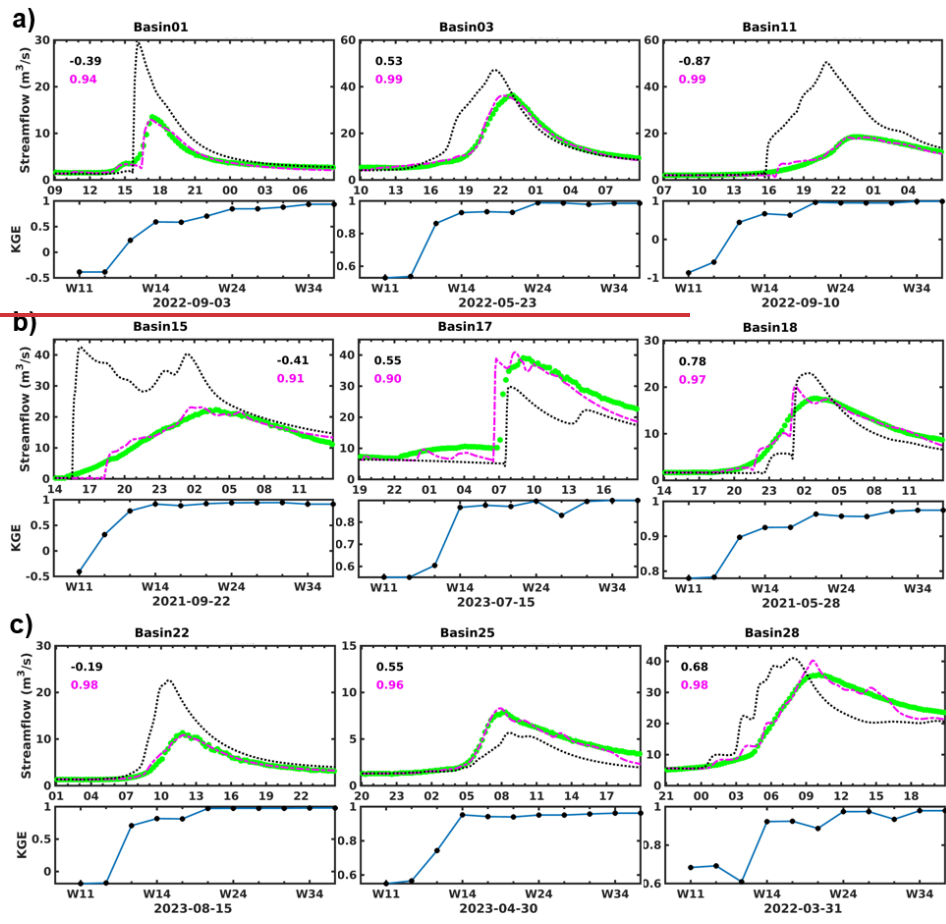
1397

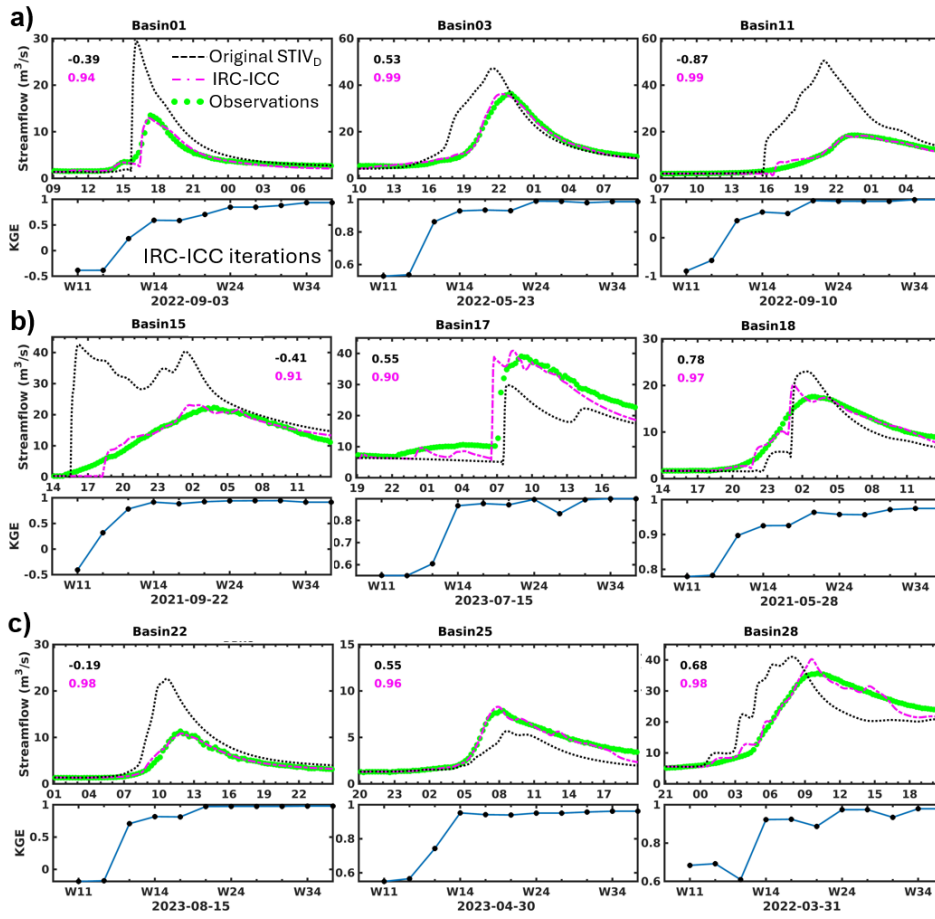


1398 **Figure 8** – The IRC-ICC performance in Basin05 as an example for the 2017-10-23 event  
 1399 (Basin05: Cataloochee Creek Basin, NC). This event is part of the 2017 Hurricane Nate. This  
 1400 figure contains **a**) hydrological responses when precipitation forcing is the STIV<sub>DBKC</sub>. The dashed  
 1401 rectangular plot consisting of intermediate results including each iteration from the IRC-ICC

1402 framework (Figure 3). **b)** the hydrological equilibrium of the IRC-ICC after 5 iterations. This  
1403 figure is adapted from Liao and Barros (2025b).

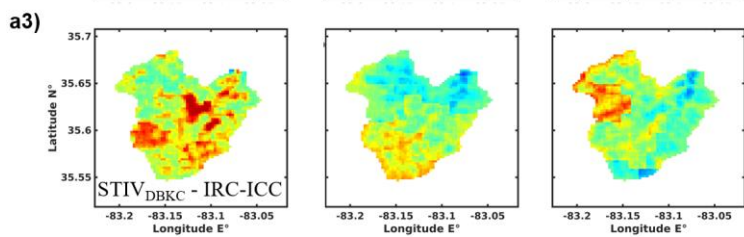
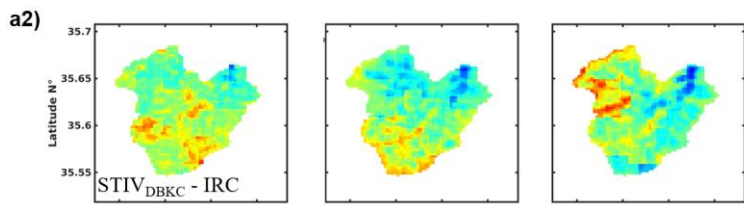
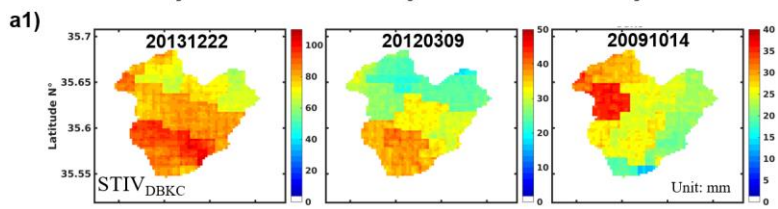
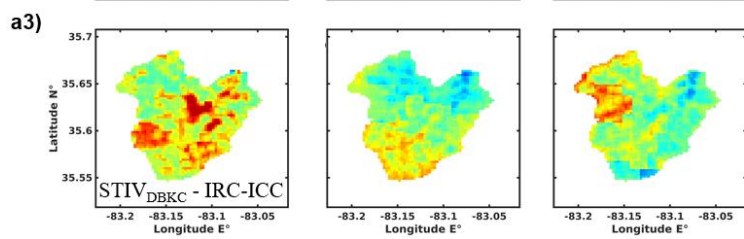
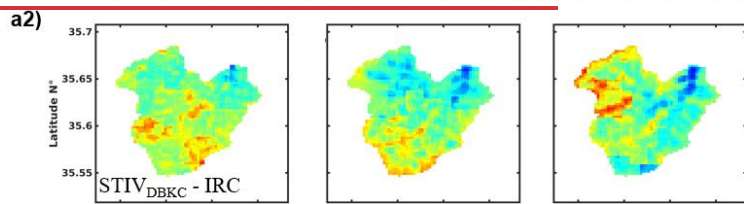
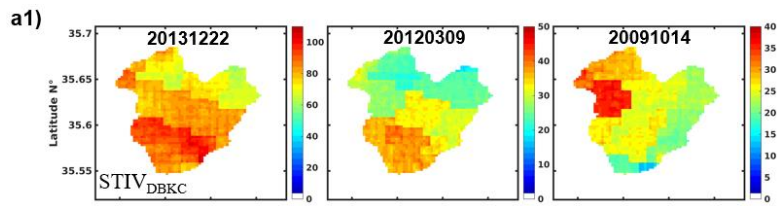
1404

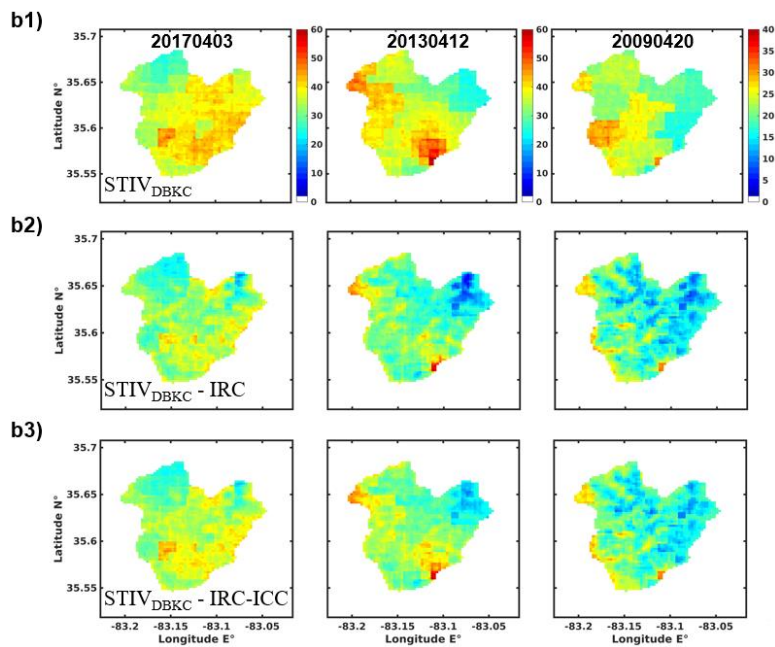




1406

1407 **Figure 9** – The IRC-ICC performance for different subregions, include **a)** 3 events from the  
 1408 Southern Appalachians; **b)** 3 events from the Central Appalachians; and **c)** 3 events from the  
 1409 Northern Appalachians. The IRC-ICC KGE evolution plots from iterations are included below the  
 1410 hydrographs. The black and pink line are from the original STIV<sub>D</sub> and the IRC-ICC equilibrium  
 1411 state (STIV<sub>D</sub><sup>IRC\*</sup>), respectively, and KGE values are displayed as colored numbers in the top left  
 1412 corners. This figure is adapted from Liao and Barros (2025b).

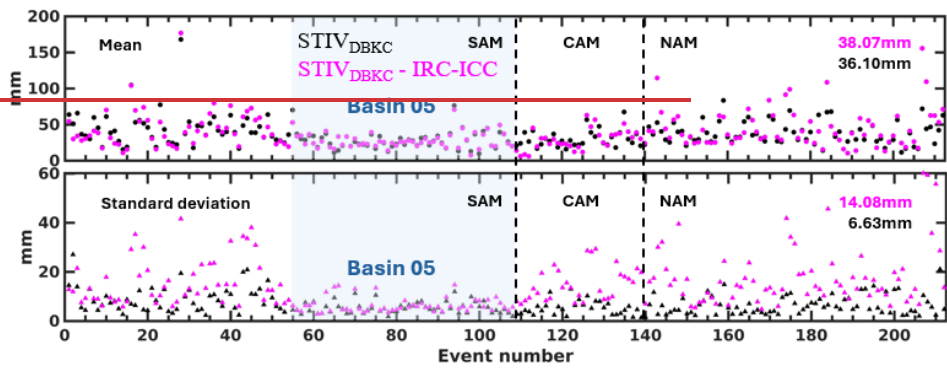




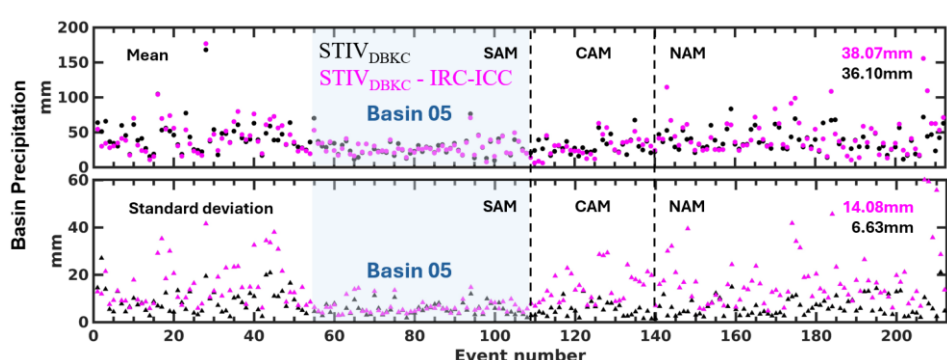
1415  
 1416 **Figure 10** – Event total precipitation maps for three cold season events (**a**) and three warm season  
 1417 events (**b**). Each column represents one event, and each row represents one precipitation product:  
 1418 STIV<sub>DBKC</sub>, STIV<sub>DBKC</sub><sup>IRC\*</sup> from IRC-only framework, and STIV<sub>DBKC</sub><sup>IRC\*</sup> from the coupled IRC-ICC  
 1419 framework. This figure is adapted from Liao and Barros (2025b).  
 1420

1421

1422



1423

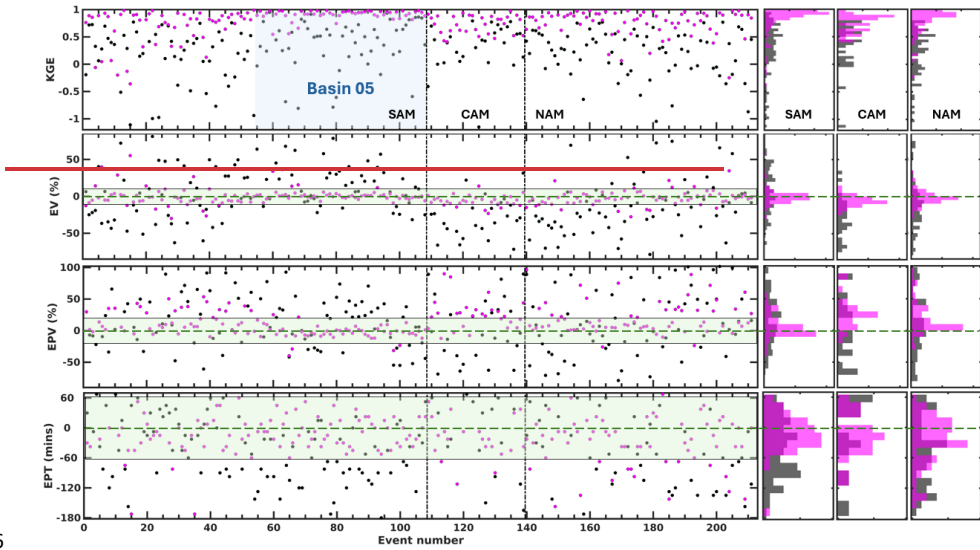


1424

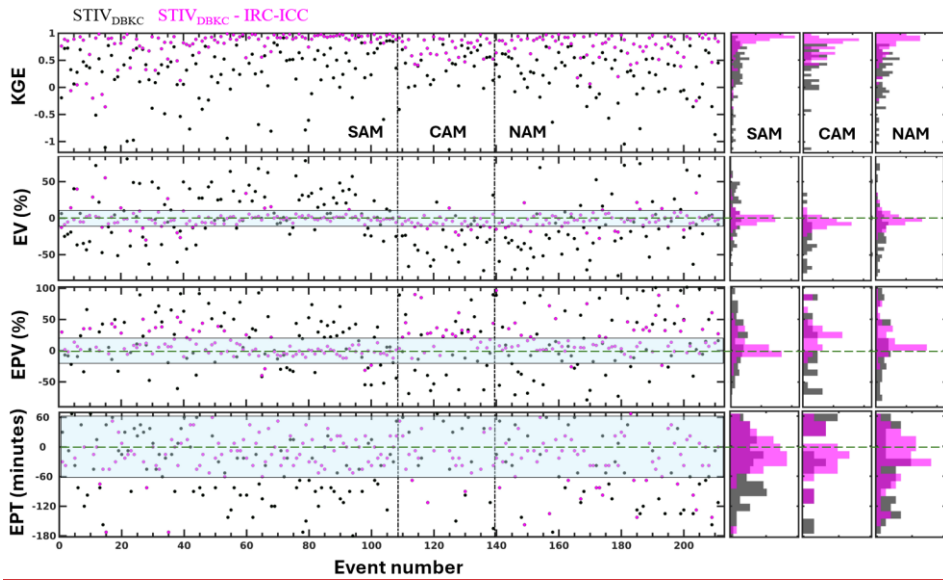
1425 **Figure 11** – Summary charts of precipitation statistics for all event-total precipitation maps. Basin  
 1426 precipitation average and standard deviation for each event are represented by circles and triangles  
 1427 in the top and bottom panel, respectively. Each panel consists of 3 sub-regions by vertical black  
 1428 lines: the Southern Appalachian Mountains, Central Appalachian Mountains, and Northern  
 1429 Appalachian Mountains. The list of events in Basin 05 (with event number ranging from 55 to  
 1430 108) in the SAM is highlighted by a blue rectangle for further discussion in the text. The average  
 1431 values of all events for both the mean and the standard deviation are calculated and shown in the  
 1432 top right corner. Black color and pink color represent pre and post IRC-ICC QPE statistics,  
 1433 respectively.

1434

1435



1436

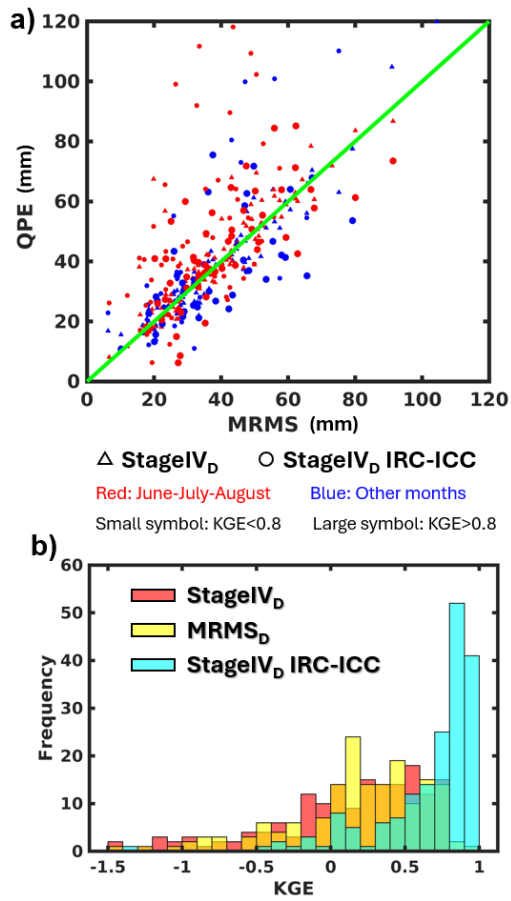


1437

1438 **Figure 12** – Summary of hydrologic skills. Green dashed lines and associated uncertainty  
1439 envelopes are only for visual illustration. Hydrologic statistics are explained in Table 2. Pink and  
1440 black scatters (each scatter represent one event) represent IRC-ICC, and baseline outputs,  
1441 respectively. Each horizontal panel is split into 3 subsections by vertical black lines representing

1442 the 3 subregions. Histograms graphs on the right hand side are provided for a summary view. This  
1443 figure is adapted from Liao and Barros (2025b).

1444



1445

1446 **Figure 13** – a) Event total QPE plots for various QPE datasets conditional on seasons and KGE  
 1447 values; b) KGE distributions across events using different QPE datasets. This figure is adapted  
 1448 from Liao and Barros (2025b).

1449